

WavesFM: Hierarchical Representation Learning for Longitudinal Wearable Sensor Waveforms

Peng Cao^{1,2,*}, Zhijian Yang^{1,*†}, Tennison Liu^{1,*†}, Jonathan Wang¹, Jiang Wu¹, Magdalena Proszewska¹, Arvind Pillai¹, Mingwu Gao¹, Amir Farjadian¹, Lawrence Cai¹, Emily Blanchard¹, Daniel McDuff¹, Pramod Rudrapatna¹, Matthew Thompson¹, Anupam Pathak¹, Mark Malhotra¹, Shwetak Patel^{1,3}, Dina Katabi², Paolo Di Achille^{1,◦,†} and Ming-Zher Poh^{1,◦,†}

*Equal contributions, ◦Joint supervision, †Corresponding Author, ¹Google Research, ²MIT, ³University of Washington

Wearable sensors enable the continuous acquisition of high-resolution physiological waveforms, such as photoplethysmography (PPG) and accelerometry (ACC), under free-living conditions. However, inferring health-related phenotypes from these signals presents significant challenges due to high sampling frequencies, multimodal dependencies, and extreme sequence lengths (e.g., weeks of recordings), compounded by a scarcity of ground-truth labels. To address these challenges, existing *self-supervised learning* (SSL) methodologies typically follow two paradigms: (1) learning rich *morphological* representations from short waveform segments while collapsing longitudinal dynamics through simple aggregation, or (2) modeling *behavioral* patterns from coarse, hand-crafted features (e.g. heart rate, step counts) spanning longer horizons but foregoing subtle, predictive signatures in raw waveforms. To bridge this gap, we propose WavesFM, a foundation model utilizing a two-stage SSL framework for longitudinal physiological data. Specifically, we decompose the learning problem into two stages: first, a segment-level encoder is pretrained to extract local embeddings from short waveforms; subsequently, a temporal encoder is trained to model the sequence of these embeddings across a multi-day horizon. This hierarchical approach overcomes the computational complexity of high-resolution, long-sequence data, allowing the overall model to capture both local signal semantics and the complex circadian and inter-day variations governing physiological dynamics. Pretrained on over 6.8M hours ($N=324k$ individuals) of recordings for the first stage and 5.3M hours ($N=10k$) for the second stage, WavesFM demonstrates superior performance across 58 diverse tasks spanning demographics, lifestyle, health conditions, and medications.

1. Introduction

The digitization of human physiology via wearable biosensors (e.g., photoplethysmography [PPG] and accelerometry [ACC]) is shifting modern healthcare from episodic snapshots to continuous, free-living monitoring for weeks or months at a time [1, 2]. These high-resolution longitudinal data offer an unprecedented window into multi-scale physiological dynamics, capturing rhythms that span orders of magnitude—from millisecond-scale heartbeat morphology to 24-hour circadian and multi-day homeostatic rhythms [3–5]. Clinically meaningful phenotypes are defined not by static values, but by *dynamic trajectories* over intra- and multi-day horizons [6–8].

Translating these trajectories into clinical insights is hindered by two bottlenecks. First, the *computational receptive field* required to process multimodal high-resolution signals over long horizons is prohibitively large (e.g., a single 100 Hz sensor yields roughly 10^8 data points per week). Second, a profound *signal-label asymmetry* exists between dense data streams and scarce subject-level clinical annotations, making end-to-end supervised learning infeasible. While *self-supervised learning* (SSL) partially mitigates label scarcity, effectively distilling high-resolution, long-sequence waveforms into discriminative embeddings remains an open challenge.

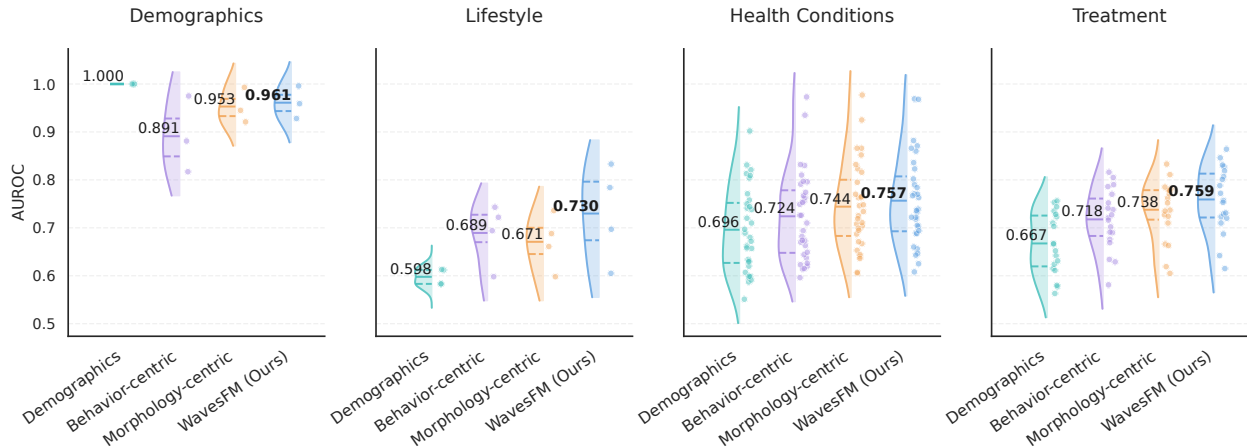


Figure 1 | **Downstream performance by category.** Compared to behavior-centric and morphology-centric approaches, WavesFM achieves superior performance across diverse downstream task categories by jointly modeling local morphology and longitudinal structure via two-stage hierarchical SSL.

Significant progress has been made in developing foundation models for wearable biosignals via SSL. These methodologies typically diverge into two paradigms to handle high-dimensional longitudinal data, exposing a fundamental *resolution trade-off*. On the one hand, *morphology-centric* approaches extract rich representations from short waveform segments (e.g. seconds to minutes) [9–16] but collapse long-term dynamics via simple pooling. This treats multi-day data as an unordered “bag of segments”, discarding vital temporal dependencies. Conversely, *behavioral-centric* approaches capture long horizons by operating on coarse, aggregated metrics like minute-level mean heart rate or hourly step counts [17–19]. While computationally scalable, this abstraction sacrifices subtle, predictive physiological signatures embedded within raw waveforms. Consequently, joint modeling high-frequency morphology and long-term longitudinal structure remains an unresolved challenge.

Here, we introduce WavesFM, a foundation model that reconciles this trade-off by decoupling local morphological encoding from long-horizon temporal modeling within a hierarchical SSL framework. Stage I comprises a *segment encoder* that learns local, multimodal representations of high-frequency PPG and ACC segments via subject-contrastive learning. In Stage II, a *temporal encoder* is trained to model the temporal dynamics of these segment-level embeddings over multi-day horizons using a masked reconstruction objective. To prevent the model from exploiting shortcuts inherent in latent-space masked modeling, we architecturally introduce a dual-branch decoder and multi-scale sparse masking. WavesFM yields a unified, subject-level embedding that integrates micro-scale morphology with macro-scale rhythms, bypassing the need to sacrifice resolution for context.

Contributions. As such, the main contributions of this work are as follows:

1. **Technically**, we introduce WavesFM, a hierarchical foundation model decoupling local morphological encoding from long-horizon temporal modeling, trained via a two-stage SSL framework that combines morphological subject-contrastive objectives with masked embedding prediction.
2. **Conceptually**, we demonstrate that resolving the trade-off between micro-scale waveform morphology and macro-scale temporal rhythms leads to more accurate capture of health phenotypes.
3. **Empirically**, through large-scale validation across 58 downstream tasks spanning demographics, health conditions, and medications, we demonstrate that WavesFM consistently outperforms existing models alongside morphological and behavioral approaches. We show the learned representations effectively capture physiologically grounded temporal variations and are robust to temporal missingness, crucial for health phenotyping in continuous wearable monitoring.

Table 1 | Comparison of WavesFM with existing paradigms in wearable sensor representation learning.

Paradigm	Key References	Input Fidelity (Resolution)	Local Modeling	Temporal Context	Temporal Modeling
Morphology-Centric	[9–16]	High: Raw Waveforms (64-100 Hz)	Self-supervised	Short: 10-60 sec	Mean Pooling (Stateless)
Behavior-Centric	[17–19]	Low: Minute-hourly features (e.g., HR, steps)	Handcrafted features	Medium: 5-24 hr Long: 1 week	Self-supervised (Stateful)
Hierarchical SSL	WavesFM (Ours)	High: Raw Waveforms (100 Hz)	Self-supervised	Long: 1 week	Self-supervised (Stateful)

2. Preliminaries

2.1. Problem Definition

Setup. Let $\mathbf{x} \in \mathbb{R}^{C \times L}$ represent a multi-day physiological recording, where C denotes the number of concurrent sensor channels (e.g., PPG and ACC). The total sequence length L is defined by the recording duration T (in seconds) and sampling frequency f_s , such that $L = T \times f_s$. We assume access to a large-scale unlabeled dataset $\mathcal{D}_u = \{\mathbf{x}_j\}_{j=1}^N$ containing N distinct temporal sequences, collected across subjects and disjoint time intervals. Additionally, we consider a smaller labeled dataset $\mathcal{D}_l = \{(\mathbf{x}_j, y_j)\}_{j=1}^M$, where y_j denotes a subject-level health phenotype (e.g., a clinical diagnosis). Reflecting the real-world scarcity of health annotations, we assume $M \ll N$.

Temporal decomposition. To handle the multi-scale nature of physiological data, we partition the global sequence \mathbf{x} of length L into a sequence of K non-overlapping *segments* $\mathcal{S} = \{\mathbf{s}_1, \mathbf{s}_2, \dots, \mathbf{s}_K\}$, where each segment $\mathbf{s}_k \in \mathbb{R}^{C \times l}$ captures a short window of duration $\tau \ll T$ (e.g., 15 seconds). Here $l = \tau \times f_s$ is the local segment length and $K = L/l$ is the total number of segments.

Learning problem. Our objective is to learn a parameterized model $f_\theta : \mathbb{R}^{C \times L} \rightarrow \mathbb{R}^d$ using \mathcal{D}_u that maps the high-dimensional raw signal \mathbf{x} to a fixed d -dimensional representation $\mathbf{z} \in \mathbb{R}^d$. This representation ideally captures both local morphological signatures and global longitudinal structure over the horizon T . For a given downstream task, we learn a task-specific head $h_\xi : \mathbb{R}^d \rightarrow \mathcal{Y}$ that maps the frozen embedding \mathbf{z} to the label space \mathcal{Y} using the labeled dataset \mathcal{D}_l .

Learning challenges. The learning problem is constrained by two primary factors:

1. **Computational complexity.** The input complexity of longitudinal sequences is $O(C \cdot L)$. For reference, a week-long recording at $f_s = 100\text{Hz}$, $L = 604,800$ seconds \times 100Hz produces $\approx 6 \times 10^7$ samples. Naive end-to-end processing of such sequences is computationally intractable.
2. **Label scarcity.** The imbalance between input dimensionality $C \times L$ and the number of labels M precludes effective supervised learning, necessitating self-supervised approach to learn meaningful physiological and behavioral priors.

2.2. Wearable Biosignals

Driven by their low power consumption, consumer wearables have largely converged on two primary biosensor modalities [20, 21]: photoplethysmography (PPG) to measure blood volume changes, and tri-axial accelerometry (ACC) to track kinematic motions and posture. These modalities are frequently paired, as ACC provides a reference to isolate motion artifacts [22], and their combination captures the coupling between physical exertion and cardiovascular response [23, 24].

Timescales. We model these signals jointly across two distinct scales, τ and L , aligned with underlying

biological and behavioral rhythms. We set the local segment window τ to 15 seconds, an epoch duration sufficient to encompass multiple cardiac cycles and resolve heartbeat morphology [25]. This window is also sufficient to characterize stationary behavioral states and consistent kinematic patterns, such as a consistent gait or posture [26]. We define the global temporal horizon L as one week. While a 24-hour window captures circadian oscillations (e.g., sleep-wake cycles), a seven-day horizon observes circaseptan patterns [27], including variations between workdays and weekends and crucial to disambiguating transient lifestyle fluctuations from invariant health phenotypes [28, 29].

2.3. Related Works

Recent years have witnessed substantial efforts toward self-supervised foundation models for wearable biosignals. These methods vary fundamentally in how they manage the extreme sequence lengths L inherent in physiological data. This divergence has created a *resolution trade-off*, where existing works prioritize either high-frequency morphological resolution or longitudinal behavioral context, but rarely both. We summarize key distinctions to prior works in Table 1.

Morphology-centric models focus on learning representations from short segments \mathbf{s}_k (typically, $\tau \in [10s, 5m]$). For approaches that only consider PPG modeling, research has shown that self-supervised pretraining on large-scale data can encode rich cardiovascular, metabolic, and demographic information [9, 12]. One predominant paradigm is contrastive learning, where distinctions are drawn regarding how positive pairs are constructed, including quality-invariance [30], morphology-aware contrast [11], and cross-model supervision from paired ECG [13]. Beyond contrastive objectives, alternative approaches have explored generative autoregressive training [14], masked reconstruction [15], and multimodal masking [16]. In the domain of accelerometry modeling, approaches employ pretext task prediction [31], relative contrastive learning [32], and knowledge distillation [10]. To our knowledge, no existing foundation model leverages joint modeling of PPG and ACC waveforms. More crucially, while these segment-level approaches capture fine-grained morphological detail, longitudinal structure is recovered only post-hoc via simple aggregation (e.g., mean-pooling [9, 33]), which collapses the multi-day variations that are themselves clinically informative.

Behavior-centric models occupy the opposite extreme of the tradeoff, navigating the complexity of L through dimensionality reduction. Rather than modeling the raw segments $\mathbf{s}_k \in \mathbb{R}^{C \times l}$, they operate on sequences of coarse, hand-crafted features $\tilde{\mathbf{s}}_k \in \mathbb{R}^p$ (e.g., minute-level heart rate, or step-count statistics), where $p \ll C \times l$. Notable approaches include Narayanswamy et al. [17] and Xu et al. [18], which model sequences of these features across hours to a day, with the latter explicitly addressing data missingness. Other efforts have extended this line of research by aligning one-day feature matrices with natural-language captions [34], or pursuing week-long behavioral streams [19]. While these models successfully capture multi-day rhythms, they forego predictive morphological signatures (e.g., pulse morphology) that can only be resolved from raw waveforms.

3. Method

Overview. We propose WavesFM, a hierarchical foundation model designed to learn representations from week-long continuous wearable waveform data. Our architecture rests on two core principles. First, we decouple morphological encoding from temporal modeling. As physiological states are quasi-stationary at the second scale but highly dynamic over multi-day horizons, this separation allows each encoder to specialize while drastically reducing the computational burden of high-resolution processing. Accordingly, the Stage I segment encoder (Section 3.1) maps 15s multimodal waveforms into a denoised embedding space using a subject-contrastive objective [9], filtering out transient artifacts in favor of robust morphological features. Second, we model long-horizon dynamics directly

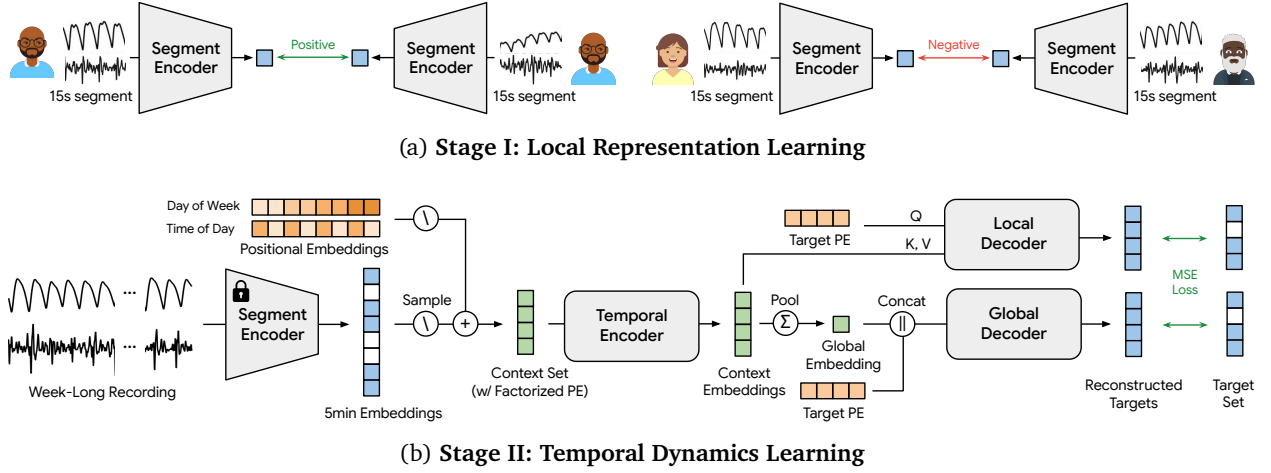


Figure 2 | **Overview of the WavesFM framework.** (a) Stage I utilizes a *segment encoder* to learn *segment embeddings* from 15-s PPG and ACC windows via subject-contrastive learning, pairing intra-subject segments against those from different individuals. (b) Stage II models long-horizon dynamics by pooling a week-long sequence of these segment embeddings into 5-minute bins, augmenting them with circadian/circaseptan positional embeddings, and passing them to a *temporal encoder* to output *temporal embeddings*. During pretraining, dual-decoder branches reconstruct held-out targets: a local branch uses cross-attention with target positional encodings, while a global branch aggregates context through a mean-pooled bottleneck. The final week-level representations are utilized for downstream health phenotyping.

within this latent space. The Stage II temporal encoder (Section 3.2) models week-long sequence of segment embeddings via masked reconstruction, focusing on high-level semantic transitions rather than fine-grained signal details. To encourage meaningful temporal modeling, we employ multi-scale temporal masking alongside a dual-branch decoder. Figure 2 visualizes the overall framework.

3.1. Stage I: Representation Learning on Multimodal Waveform Segment

The objective of Stage I is to map high-resolution multimodal segments $\mathbf{s}_k \in \mathbb{R}^{C \times l}$ into a d -dimensional latent space that preserves morphological features while suppressing stochastic noise. By training on short $\tau = 15$ s windows, we ensure that segment encoder e_ϕ captures locally stationary features (e.g., dirotic notch in PPG or gait rhythm in ACC).

Subject-contrastive objective. Standard contrastive frameworks often rely on aggressive data augmentation (e.g., jittering, scaling) to create positive pairs. While effective for images with strong spatial correlation, these transformations can inadvertently destroy subtle physiological signatures in physiological waveforms. To circumvent this, we define positive pairs as temporally disjoint segments sampled from the same subject, while negative pairs are segments sampled from different subjects. This formulation forces the model to learn to differentiate subject-specific physiological identity. Formally, let $\text{id}(\mathbf{s})$ denote the unique subject identity from which the segment \mathbf{s} was sampled. A pair $(\mathbf{s}_i, \mathbf{s}_j)$ is then a positive pair if $\text{id}(\mathbf{s}_i) = \text{id}(\mathbf{s}_j)$ and $i \neq j$ [9].

The segment encoder $e_\phi : \mathbb{R}^{C \times l} \rightarrow \mathbb{R}^d$ maps a segment \mathbf{s}_k to an embedding $\mathbf{e}_k = e_\phi(\mathbf{s}_k)$. This embedding is projected to a contrastive manifold via a projection head $g_\omega : \mathbb{R}^d \rightarrow \mathbb{R}^{d'}$, such that $\mathbf{q}_k = g_\omega(\mathbf{e}_k)$, where \mathbf{q}_k is also ℓ_2 -normalized. Concretely, for a batch of B segments, let $\mathcal{I} = [B]$ be the set of indices. For an anchor segment $i \in \mathcal{I}$, we denote the set of positive indices $\mathcal{P}(i) = \{j \in \mathcal{I} \setminus \{i\} : \text{id}(\mathbf{s}_i) = \text{id}(\mathbf{s}_j)\}$. The contrastive loss for anchor i is then [35, 36]:

$$\mathcal{L}_i^{\text{Stage I}} = -\frac{1}{|\mathcal{P}(i)|} \sum_{j \in \mathcal{P}(i)} \log \frac{\exp(\mathbf{q}_i \cdot \mathbf{q}_j / \gamma)}{\sum_{a \in \mathcal{I} \setminus \{i\}} \exp(\mathbf{q}_i \cdot \mathbf{q}_a / \gamma)}, \quad (1)$$

where γ is the temperature hyperparameter. This objective forces the latent space to cluster by invariant physiological traits, effectively performing a semantic denoising step where only stable and robust morphological features are preserved. After Stage I pretraining, the projection head g_ω is discarded, and the encoder e_ϕ is frozen to produce segment embeddings for Stage II.

3.2. Stage II: Temporal Dynamics Learning via Masked Embedding Prediction

Stage II trains a temporal encoder e_ψ to model the longitudinal evolution of physiological states over a one-week horizon. While Stage I embeddings capture local morphology, the temporal encoder captures macro-scale rhythms including circadian oscillations, sleep-wake transitions, and circaseptan (weekly) behavioral shifts. Specifically, $e_\psi : \mathbf{V} \mapsto \mathbf{z}$ maps a sequence of M latent states $\mathbf{V} = [\mathbf{v}_1, \dots, \mathbf{v}_M]^T \in \mathbb{R}^{M \times d}$ to a sequence-level representation $\mathbf{z} \in \mathbb{R}^d$.

Challenges of masked modeling on embedding sequences. Directly applying a masked-prediction objective to embedding sequences risks two failure modes that bypass meaningful temporal modeling: (i) *Interpolation shortcut*: because slow-varying physiological states exhibit high temporal autocorrelation, missing embeddings can be trivially reconstructed from visible neighbors; (ii) *Identity shortcut*: the encoder can degenerate into an identity function, passing context embeddings straight through to the decoder to perform heavy lifting and resolve target reconstruction. We break the interpolation shortcut at the input stage using an aggressive, multi-scale masking strategy that creates contiguous missing patches. Simultaneously, we eliminate the identity shortcut by using dual-branch decoders, forcing the encoder to route information through a collapsed temporal bottleneck.

Input sequence construction. To mitigate short-term redundancy and ensure computational tractability, we aggregate the K segment embeddings from Stage I into a compressed sequence of $M = 2016$ temporal bins (representing one week at 5-minute intervals). Each bin embedding \mathbf{v}_t is computed as the mean of 20 contiguous, non-overlapping Stage I embeddings. For time bins where data is missing—due to off-body periods or sensor duty-cycling—we replace \mathbf{v}_t with a learnable [MISSING] token. Conventional absolute positional encoding schemes are ill-suited for free-living data because recordings are sampled *arbitrarily* relative to the calendar; a sequence may begin at any day or time, making absolute indices semantically inconsistent across samples. To explicitly encode the nested periodicities of human physiology, we introduce a *factorized positional encoding* scheme anchored to the recording’s calendar time, allowing the model to understand biologically recurring patterns.

Let $w_t = \text{cal}(\mathbf{v}_t)$ be the calendar time of each embedding. We map w_t to factorized indices via modulo functions $\sigma_{\text{dow}}(w_t) \in \{1, \dots, 7\}$ and $\sigma_{\text{tod}}(w_t) \in \{1, \dots, 288\}$, utilizing two learnable lookup tables, $\mathbf{P}_{\text{dow}} \in \mathbb{R}^{7 \times d}$ and $\mathbf{P}_{\text{tod}} \in \mathbb{R}^{288 \times d}$. These represent *day-of-week* and *time-of-day* information (7 days in a week; 288 5-minute bins in a 24-hour day), thus yielding:

$$\mathbf{v}_t \leftarrow \mathbf{v}_t + (\mathbf{P}_{\text{dow}})_{\sigma_{\text{dow}}(w_t),:} + (\mathbf{P}_{\text{tod}})_{\sigma_{\text{tod}}(w_t),:} \quad (2)$$

This factorization ensures that embeddings from identical calendar periods share the same positional encoding regardless of sequence index, injecting circadian/circaseptan priors into the temporal model.

Multi-scale masking. To break the interpolation shortcuts inherent in autocorrelated longitudinal sequences, we employ an aggressive masking strategy. From the full sequence of M embeddings, we sample a sparse *context set* \mathbf{C} of size $N_{\text{ctx}} = 252$ (approximately 12.5% of the weekly horizon) to serve as input to the temporal encoder e_ψ . The sampling of \mathbf{C} follows a *multi-scale patching protocol* designed to capture dynamics across different temporal resolutions. For each training sample, we randomly draw a patch size $P \sim \text{Uniform}(\{1, 2, 4\})$, corresponding to random patches of 5, 20, 60-minutes, respectively. We then partition the index set $\{1, \dots, M\}$ into M/P non-overlapping contiguous patches; and randomly sample N_{ctx}/P patches to form the context set. The target set is then $\mathbf{T} = \mathbf{V} \setminus \mathbf{C}$. This

multi-scale strategy serves dual purposes: small patches forces the model to resolve fine-grained physiological transitions, such as sleep-stage shifts or instantaneous activity changes, while larger patches create extended missingness that demand multi-hour context integration, removing the dense-neighbor structure that interpolation relies on.

Dual-branch reconstruction. The context sequence, augmented with factorized positional encodings, is processed by the temporal encoder—a stack of Transformer blocks [37]—to produce sequence-level context embeddings. To eliminate the interpolation shortcut inherent in highly redundant time-series data, we decode these embeddings through two complementary branches with distinct geometric constraints: (i) a *local* branch: a standard cross-attention decoder where target positional embeddings query the context embeddings to reconstruct each target position; (ii) a *global* branch: the context embeddings are mean-pooled along the temporal dimension into a single d -dimensional week-level vector. This global descriptor is then concatenated with the target positional encodings and processed by a Transformer decoder to reconstruct the missing targets.

By collapsing the temporal sequence into a single bottleneck vector, the global decoder branch cannot perform localized lookups from adjacent unmasked bins, requiring the temporal encoder successfully compresses week-long health dynamics into a summary vector. Conversely, as relying solely on this bottleneck would over-smooth the latent space, the local decoder branch provides dense, per-token gradients for the temporal encoder to preserve fine-grained temporal structures.

Reconstruction objective. We minimize the MSE between the ground-truth and predicted target embeddings. Let $\mathcal{M} \subset [M]$ be the set of indices for reconstruction targets in \mathbf{T} , the combined loss is:

$$\mathcal{L}^{\text{Stage II}} = \underbrace{\frac{1}{d \cdot |\mathcal{M}|} \sum_{t \in \mathcal{M}} \|\mathbf{v}_t - \hat{\mathbf{v}}_t^l\|_2^2}_{\text{Local branch loss}} + \underbrace{\frac{1}{d \cdot |\mathcal{M}|} \sum_{t \in \mathcal{M}} \|\mathbf{v}_t - \hat{\mathbf{v}}_t^g\|_2^2}_{\text{Global branch loss}} \quad (3)$$

where $\hat{\mathbf{v}}_t^l, \hat{\mathbf{v}}_t^g$ are the corresponding reconstructions from the local and global branches respectively.

Downstream use. At inference time, a week-long signal is processed end-to-end: 15s segments are encoded by the segment encoder, mean-pooled into 5-minute bins, augmented with factorized positional embeddings, and passed through the temporal encoder. The resulting week-level embedding produced by the global decoder branch serves as final representations for downstream probing.

4. Experiments

Pretraining and evaluation datasets. We implemented WavesFM and trained it on an extensive de-identified, unlabeled dataset of PPG and ACC waveforms. All participants provided voluntary consent for the use of their de-identified data, and a secondary research exemption was obtained from an Institutional Review Board (IRB). We used 6.8M hours of intermittently sampled waveforms from 324k individuals to train Stage I, and a subset of this data, 5.3M hours from 61.2k week-long recordings ($N=10k$ individuals), to train Stage II. Downstream task probing and testing were conducted on a held-out dataset of 11,736 participants, collected under informed consent from the Fitbit Hypertension Study using an IRB-approved study protocol, with an average of 11.7 weeks of data per subject. Data was split at the subject level (70/15/15 for train/val/test) to prevent data leakage. This evaluation set includes 58 self-reported labels spanning demographics, lifestyle behaviors, health conditions, and treatments. More details on data splits and preprocessing are included in Appendix B.

Baselines. To evaluate the empirical performance of WavesFM, we compare it against two baselines representing the dominant paradigms in wearable representation learning, both trained on our

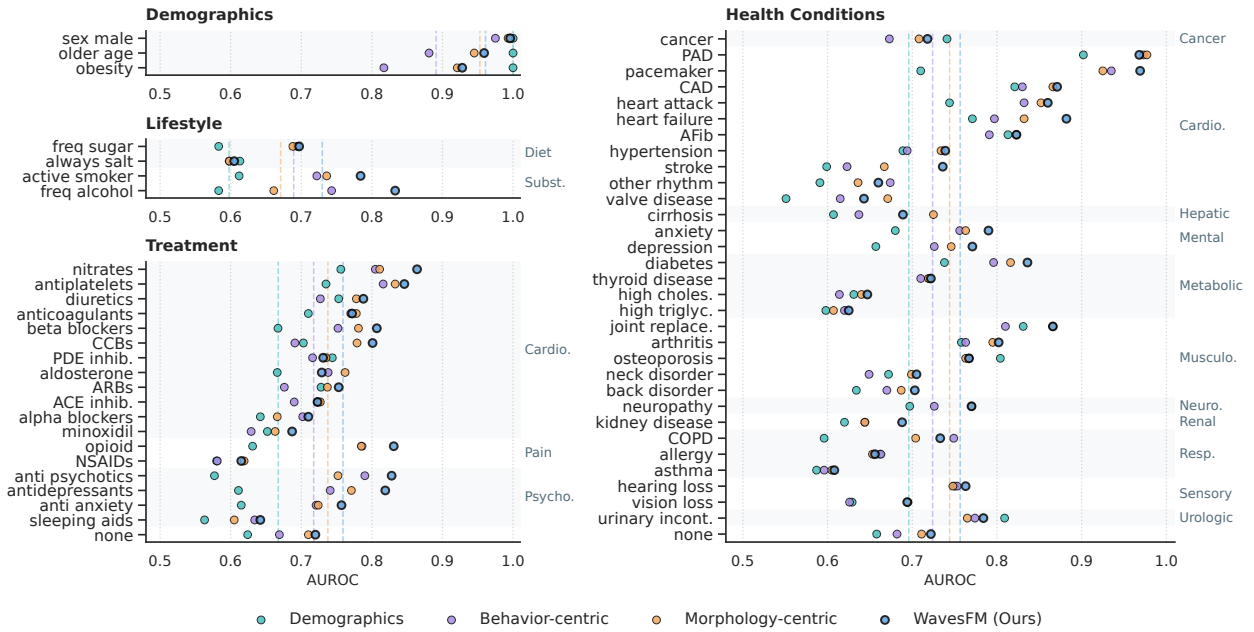


Figure 3 | **WavesFM outperforms baselines across clinical prediction tasks.** Test-set AUROC across demographics, lifestyle, treatment and health condition tasks are reported. Tasks are grouped by clinical categories (right-side labels); dashed lines mark per-panel mean AUROC for each model.

dataset and constructed using components of our framework to isolate the contribution of hierarchical modeling from confounders such as pretraining data or model capacity: (i) a *Morphology-Centric* baseline that mean-pools the frozen Stage I segment embeddings into a subject-level representation, preserving local signal fidelity but discarding multi-day temporal dynamics; and (ii) a *Behavior-Centric* baseline that replaces our Stage I segment embeddings with handcrafted features derived using NeuroKit2 [38] (e.g., heart rate, heart rate variability, motion metrics) and trains our Stage II temporal encoder on top, capturing multi-day behavioral shifts but forfeiting fine-grained morphological resolution. To establish a reference for predictive difficulty of each task, we additionally evaluate a demographics-only model using age, sex, and BMI as features. We also benchmark against supervised temporal aggregators trained directly on unpooled Stage-I embedding sequences and open-weight public PPG foundation models [11–13]. Baseline implementation details are reported in Appendix C.

Evaluation protocol. We formulate each of the 58 labels as a binary classification task and evaluate all models under a standard linear probing protocol on top of frozen subject-level embeddings. For the morphology-centric baseline, subject-level embeddings are obtained by mean-pooling all segment embeddings across each subject’s recordings. For the behavior-centric baseline and WavesFM, week-level embeddings are extracted from the frozen temporal encoder for each available week and then averaged across all weeks per subject to yield a single subject-level representation. For each task, we train an ℓ_2 -regularized logistic regression, tuning the regularization strength on validation set. Final performance is reported on the held-out test set. We report AUROC as our primary metric in the main text; to assess statistical robustness, each metric is averaged over 1,000 bootstrap resamples of the test set, with means reported in the main text and 95% confidence intervals together with the partial AUROC (pAUC) at a 10% false positive rate (FPR) threshold reported in Appendix D.

4.1. WavesFM Outperforms Morphology- and Behavior- Centric Baselines

Figure 3 shows downstream performance across all 58 tasks. All physiology-based paradigms substantially exceed the demographics-only reference, confirming that wearable signals carry health-relevant

information beyond age, sex, and BMI. WavesFM achieved the best average rank of 1.44 (Figure 10), outperforming all baseline models by a statistically significant margin under a post-hoc Nemenyi test ($\alpha = 0.05$, $CD = 0.616$), and surpassing the behavior-centric baseline on 52 of 58 tasks (89.7%) and the morphology-centric baseline on 46 of 58 tasks (79.3%). Across categories (Figure 1), WavesFM yields mean AUROC improvements of +7.0 points on demographics, +4.1 on lifestyle, +3.3 on health conditions, and +4.1 on treatment over the behavior-centric baseline, with corresponding gains over the morphology-centric baseline of +0.8, +5.9, +1.3, and +2.1, respectively.

Notably, the largest gains over the behavior-centric baseline are found on tasks whose predictive signatures may live in waveform morphology: obesity (0.817→0.928, +13.6%), calcium channel blocker (CCB) use (0.691→0.801, +15.9%) and angiotension receptor blocker (ARB) use (0.676→0.753, +11.4%). Obesity is associated with increased arterial stiffness [39] whereas CCB and ARB reduce vascular resistance and pulse wave reflections [40], changing the PPG waveform morphology which cannot be captured by minute-level statistical features. Conversely, the largest gains over the morphology-centric baseline concentrate on tasks whose signatures unfold over multi-day horizons rather than within individual segments, such as frequent alcohol use (0.661→0.833, +26.0%) and antipsychotics use (0.752→0.828, +10.1%). These phenotypes may manifest as transient changes in the PPG waveform along with disruptions in circadian rhythms [41] or sleep architecture [42] that segment-level mean-pooling cannot resolve, but that the temporal encoder captures by integrating context across the full week-long horizon. Together, these results demonstrate that jointly modeling micro-scale morphology and macro-scale temporal rhythms improves health phenotyping.

Learned temporal dynamics. To understand the representations driving these gains, particularly against the stronger morphology-centric baseline, we analyzed the unpooled, week-long embedding sequences at a 5-minute resolution. Specifically, we compared the baseline’s aggregated Stage I segment embeddings against the per-token outputs of WavesFM’s Stage II temporal encoder. As shown in Figure 4, the Stage I embeddings produces a shallow binary pattern: similarity remains tightly clustered throughout the daytime hours and dips during sleep, indicating that segment-level morphology alone resolves little beyond a sleep/wake contrast. The Stage II embeddings, in contrast, exhibit a continuous, full-cycle circadian rhythm—similarity peaks sharply at the 9–10 AM reference window each day and descends smoothly to nighttime, recovering the physiological transitions that unfold between waking, peak activity, and rest. The weekday-to-weekend shift is also visible as a slight flattening of the Saturday–Sunday peaks, consistent with altered routines on non-work days. More analyses are included in Appendix D.5, showing that the factorized positional embeddings recover circadian and circaseptan structure (Figure 13) and that the rhythmic geometry persists under alternative reference anchors and across inter-segment time distances (Figure 14). Together, these confirm the temporal encoder’s ability to model temporal dynamics across multiple scales, explaining WavesFM’s superiority on the tasks characterized by temporal variations.

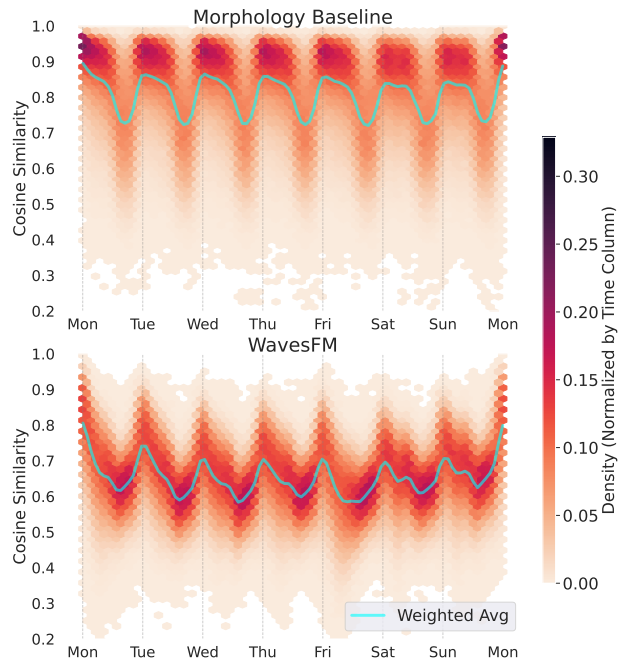


Figure 4 | **Stage II embeddings exhibit stronger circadian structure.** Hexbin distributions of pairwise cosine similarities across the week, referenced to each subject’s Monday 9–10 AM bin.

4.2. Robustness to Longitudinal Missingness

Wearable recordings are routinely incomplete due to duty-cycling and irregular wear, so we evaluated each model under five systematic missingness scenarios: the entire week, daytime (9AM–9PM) only, nighttime (12AM–6AM) only, weekdays only, and weekends only. As shown in Figure 5, WavesFM achieves the highest mean AUROC across every scenario. The most challenging condition for all three models is night-only, where reduced physiological variance limits the discriminability of health-relevant signals; nonetheless, WavesFM’s AUROC drops by 3.3% (0.767→0.742) relative to the full-week baseline, compared to 4.1% for the morphology-centric baseline (0.750→0.719) and 4.7% for the behavior-centric baseline (0.729→0.695). A similar larger drop of 1.8% is seen in the behavior-centric model during weekends (0.729→0.716), potentially due to disrupted macro-behavioral routines, whereas WavesFM further demonstrates robustness with a drop of only 0.8% (0.767→0.761) by successfully capturing complementary high-resolution morphology. Per-category breakdowns for longitudinal missingness are included in Appendix D.2.

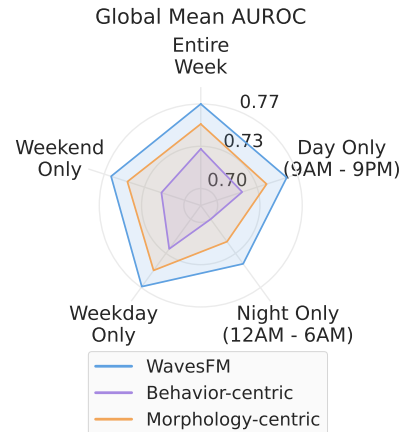


Figure 5 | Performance across longitudinal missingness.

4.3. Hierarchical SSL Outperforms Supervised Baselines Under Label Scarcity

Since self-supervised temporal pretraining is motivated by the label-scarcity that characterizes wearable cohorts, we compare linear probing on WavesFM’s pretrained embeddings against supervised temporal aggregators (e.g., an LSTM, cross-attention, or weighted pooling) trained directly on the frozen Stage I segment embeddings under label-scarce settings. We trained both the linear probe and each supervised aggregator on a 10% subject-level subset of the labeled training data (1k subjects) and evaluate on the full held-out test set. As shown in Table 2 (per-task results in Table 9), none of the three aggregators matches the performance of a simple linear probe on WavesFM’s pretrained subject-level embeddings, with WavesFM achieving an average AUROC improvement of 5.2 points over the strongest supervised baseline. By absorbing long-horizon dynamics into a single label-free representation during pretraining, the temporal encoder shifts the burden of long-sequence modeling away from the downstream task, enabling efficient linear probing in the label-scarce regimes.

Table 2 | Comparison with supervised baselines trained on a 10% subset.

Method	AUROC [†]
LSTM	0.658
Weighted Pooling	0.661
Cross-attention	0.667
WavesFM	0.719

4.4. Comparison with Public PPG Foundation Models

As an additional point of comparison, we evaluate WavesFM against three publicly available PPG foundation models: PaPaGei [11], Pulse-PPG [12], and AnyPPG [13] in Appendix D.4. While WavesFM achieves stronger downstream performance, we caution against interpreting these results as a direct architectural comparison, as our evaluation cohort comes from a different data source than their pretraining data. Robust transfer across sensor hardware and recording protocols remains an open problem for wearable foundation models. Additionally, the segment encoder architectures underlying these models are largely complementary to our framework and could be substituted as the Stage I encoder, with our hierarchical Stage II providing the longitudinal modeling on top.

4.5. Ablation Studies

We empirically validate the architectural interventions introduced in Section 3.2 to prevent shortcut learning in Stage II in Appendix E. Removing either branch of the dual-branch decoder degrades performance, with the gap widening under data constraints (night-only inputs, 10% subject subsets), indicating that the two branches contribute complementary, non-redundant pressure on the encoder (Figure 15). Furthermore, aggressive context subsampling (e.g, retaining only 12.5% to 25% of the sequence) yields significantly better representation than milder masking (Figure 17), and utilizing an average-pooled segment embedding proves consistently superior to a learnable token for the week-level representation (Figure 16). Together, these confirm that our interventions are collectively necessary to close the interpolation and identity shortcuts.

5. Conclusion

In summary, we introduced WavesFM, a foundation model for multimodal PPG and ACC biosignals that effectively addresses the trade-off between high-resolution signal morphology and longitudinal temporal context. By decoupling the learning process into a hierarchical two-stage framework, WavesFM utilizes a segment encoder to robustly extract morphological features and a temporal encoder to capture the multi-scale rhythms governing human physiology. Empirical validation across a diverse suite of clinical, demographic, and lifestyle tasks confirms that WavesFM significantly and consistently outperforms existing foundation models as well as specialized morphological and behavioral paradigms. Furthermore, the learned representations demonstrate robustness to temporal missingness, which is crucial for continuous wearable monitoring. More broadly, our analyses suggest that capturing the interaction between micro-scale morphological fidelity and macro-scale longitudinal dynamics is a vital direction towards more precise health phenotyping via consumer health wearables. Limitations, future work, and societal impacts are discussed in Appendix A.

References

- [1] Jessilyn Dunn, Ryan Runge, and Michael Snyder. Wearables and the medical revolution. *Personalized Medicine*, 15(5):429–448, 2018.
- [2] Eric J Topol. High-performance medicine: the convergence of human and artificial intelligence. *Nature medicine*, 25(1):44–56, 2019.
- [3] Benjamin R Pittman-Polletta, Frank AJL Scheer, Matthew P Butler, Steven A Shea, and Kun Hu. The role of the circadian system in fractal neurophysiological control. *Biological Reviews*, 88(4):873–894, 2013.
- [4] Sandra Crnko, Bastiaan C Du Pré, Joost PG Sluijter, and Linda W Van Laake. Circadian rhythms and the molecular clock in cardiovascular biology and disease. *Nature Reviews Cardiology*, 16(7):437–447, 2019.
- [5] Kazuomi Kario. Morning surge in blood pressure and cardiovascular risk: evidence and perspectives. *Hypertension*, 56(5):765–773, 2010.
- [6] Mustafa Halimeh, Yonghua Yang, Theodore Sheehan, Solveig Vieluf, Michele Jackson, Tobias Loddenkemper, and Christian Meisel. Wearable device assessments of antiseizure medication effects on diurnal patterns of electrodermal activity, heart rate, and heart rate variability. *Epilepsy & Behavior*, 129:108635, 2022.
- [7] Heather Hall, Dalia Perelman, Alessandra Breschi, Patricia Limcaoco, Ryan Kellogg, Tracey McLaughlin, and Michael Snyder. Glucotypes reveal new patterns of glucose dysregulation. *PLoS biology*, 16(7): e2005143, 2018.

- [8] John A Berkebile, Omer T Inan, and Paul A Beach. Wearable multimodal sensing for quantifying the cardiovascular autonomic effects of levodopa in parkinsonism. *Frontiers in Network Physiology*, 5:1543838, 2025.
- [9] Salar Abbaspourazad, Oussama Elachqar, Andrew Miller, Saba Emrani, Udhyakumar Nallasamy, and Ian Shapiro. Large-scale training of foundation models for wearable biosignals. In *The Twelfth International Conference on Learning Representations*, 2024.
- [10] Salar Abbaspourazad, Anshuman Mishra, Joseph Futoma, Andrew C Miller, and Ian Shapiro. Wearable accelerometer foundation models for health via knowledge distillation. *arXiv preprint arXiv:2412.11276*, 2024.
- [11] Arvind Pillai, Dimitris Spathis, Fahim Kawsar, and Mohammad Malekzadeh. Papagei: Open foundation models for optical physiological signals. In *The Thirteenth International Conference on Learning Representations*, 2025.
- [12] Mithun Saha, Maxwell A Xu, Wanting Mao, Sameer Neupane, James M Rehg, and Santosh Kumar. Pulse-ppg: An open-source field-trained ppg foundation model for wearable applications across lab and field settings. *Proceedings of the ACM on Interactive, Mobile, Wearable and Ubiquitous Technologies*, 9(3): 1–35, 2025.
- [13] Guangkun Nie, Gongzheng Tang, Yujie Xiao, Jun Li, Shun Huang, Deyun Zhang, Qinghao Zhao, and Shenda Hong. Anyppg: An ecg-guided ppg foundation model trained on over 100,000 hours of recordings for holistic health profiling. *arXiv preprint arXiv:2511.01747*, 2025.
- [14] Zhaoliang Chen, Cheng Ding, Saurabh Kataria, Runze Yan, Minxiao Wang, Randall Lee, and Xiao Hu. Gpt-ppg: a gpt-based foundation model for photoplethysmography signals. *Physiological Measurement*, 46(5):055004, 2025.
- [15] Simon A Lee, Cyrus Tanade, Hao Zhou, Juhyeon Lee, Megha Thukral, Minji Han, Rachel Choi, Md Sazzad Hissain Khan, Baiying Lu, Migyeong Gwak, et al. Himae: Hierarchical masked autoencoders discover resolution-specific structure in wearable time series. *arXiv preprint arXiv:2510.25785*, 2025.
- [16] Xiao Gu, Wei Tang, Jinpei Han, Veer Sangha, Fenglin Liu, Shreyank N Gowda, Antonio H Ribeiro, Patrick Schwab, Kim Branson, Lei Clifton, et al. Cardiac health assessment across scenarios and devices using a multimodal foundation model pretrained on data from 1.7 million individuals. *Nature Machine Intelligence*, 8(2):220–233, 2026.
- [17] Girish Narayanswamy, Xin Liu, Kumar Ayush, Yuzhe Yang, Xuhai Xu, shun liao, Jake Garrison, Shyam A. Taylor, Jacob Sunshine, Yun Liu, Tim Althoff, Shrikanth Narayanan, Pushmeet Kohli, Jiening Zhan, Mark Malhotra, Shwetak Patel, Samy Abdel-Ghaffar, and Daniel McDuff. Scaling wearable foundation models. In *The Thirteenth International Conference on Learning Representations*, 2025.
- [18] Maxwell A Xu, Girish Narayanswamy, Kumar Ayush, Dimitris Spathis, Shun Liao, Shyam A Taylor, Ahmed Metwally, A Ali Heydari, Yuwei Zhang, Jake Garrison, et al. Lsm-2: Learning from incomplete wearable sensor data. *arXiv preprint arXiv:2506.05321*, 2025.
- [19] Eray Erturk, Fahad Kamran, Salar Abbaspourazad, Sean Jewell, Harsh Sharma, Yujie Li, Sinead Williamson, Nicholas J Foti, and Joseph Futoma. Beyond sensor data: Foundation models of behavioral data from wearables improve health predictions. In *Forty-second International Conference on Machine Learning*, 2025.
- [20] Kwang Bok Kim and Hyun Jae Baek. Photoplethysmography in wearable devices: a comprehensive review of technological advances, current challenges, and future directions. *Electronics*, 12(13):2923, 2023.
- [21] Che-Chang Yang and Yeh-Liang Hsu. A review of accelerometry-based wearable motion detectors for physical activity monitoring. *Sensors*, 10(8):7772–7788, 2010.
- [22] Jongshill Lee, Minseong Kim, Hoon-Ki Park, and In Young Kim. Motion artifact reduction in wearable photoplethysmography based on multi-channel sensors with multiple wavelengths. *Sensors*, 20(5):1493, 2020.

- [23] Laís Tonello, Felipe F Reichert, Iransé Oliveira-Silva, Sebastián Del Rosso, Anthony S Leicht, and Daniel A Boulosa. Correlates of heart rate measures with incidental physical activity and cardiorespiratory fitness in overweight female workers. *Frontiers in physiology*, 6:405, 2016.
- [24] Daivaras Sokas, Eglė Tamulevičiūtė-Prascienė, Aurelija Beigienė, Vitalija Barasaitė, Julius Marozas, Raimondas Kubilius, Raquel Bailón, and Andrius Petrėnas. Wearable-based assessment of heart rate response to physical stressors in patients after open-heart surgery with frailty. *IEEE Journal of Biomedical and Health Informatics*, 27(4):1825–1834, 2023.
- [25] Adam Sturge, Stefan van Duijvenboden, Barbara Casadei, and Aiden Doherty. Development and validation of an ecg-based 10-year risk prediction model for major adverse cardiac and cerebrovascular events in uk biobank. *medRxiv*, pages 2026–03, 2026.
- [26] Fangyu Liu, Amal A Wanigatunga, and Jennifer A Schrack. Assessment of physical activity in adults using wrist accelerometers. *Epidemiologic reviews*, 43(1):65–93, 2021.
- [27] Rochelle I De Silva, Rachel E Stirling, Jodie Naim-Feil, Shivam Puri, Elizabeth Paratz, and Philippa J Karoly. Multiday rhythms modulate human heart rate: an observational study in healthy adults. *bioRxiv*, pages 2026–03, 2026.
- [28] Monika Šimaitytė, Andrius Petrėnas, Julija Kravčenko, Eleni Kaldoudi, and Vaidotas Marozas. Objective evaluation of physical activity pattern using smart devices. *Scientific Reports*, 9(1):2006, 2019.
- [29] Chris Brooks, Nina Shaafi Kabiri, Jaspreet Bhangu, Xuemei Cai, Eve Pickering, Michael Kelley Erb, Sanford Auerbach, Paolo Bonato, Tara L Moore, Farzad Mortazavi, et al. The impact of chronotype on circadian rest-activity rhythm and sleep characteristics across the week. *Chronobiology International*, 38(11):1575–1590, 2021.
- [30] Cheng Ding, Zhicheng Guo, Zhaoliang Chen, Randall J Lee, Cynthia Rudin, and Xiao Hu. Siamquality: a convnet-based foundation model for photoplethysmography signals. *Physiological Measurement*, 45(8):085004, 2024.
- [31] Hang Yuan, Shing Chan, Andrew P Creagh, Catherine Tong, Aidan Acquah, David A Clifton, and Aiden Doherty. Self-supervised learning for human activity recognition using 700,000 person-days of wearable data. *NPJ digital medicine*, 7(1):91, 2024.
- [32] Maxwell A Xu, Jaya Narain, Gregory Darnell, Haraldur T Hallgrímsson, Hyewon Jeong, Darren Forde, Richard Andres Fineman, Karthik Jayaraman Raghuram, James Matthew Rehg, and Shirley You Ren. Relcon: Relative contrastive learning for a motion foundation model for wearable data. In *The Thirteenth International Conference on Learning Representations*, 2025.
- [33] Yu Yvonne Wu, Yuwei Zhang, Hyungjun Yoon, Ting Dang, Dimitris Spathis, Tong Xia, Qiang Yang, Jing Han, Dong Ma, Sung-Ju Lee, et al. Wearable foundation models should go beyond static encoders. *arXiv preprint arXiv:2603.19564*, 2026.
- [34] Yuwei Zhang, Kumar Ayush, Siyuan Qiao, A Ali Heydari, Girish Narayanswamy, Maxwell A Xu, Ahmed Metwally, Jinhua Xu, Jake Garrison, Xuhai Xu, et al. Sensorlm: Learning the language of wearable sensors. In *The Thirty-ninth Annual Conference on Neural Information Processing Systems*, 2025.
- [35] Aaron van den Oord, Yazhe Li, and Oriol Vinyals. Representation learning with contrastive predictive coding. *arXiv preprint arXiv:1807.03748*, 2018.
- [36] Ting Chen, Simon Kornblith, Mohammad Norouzi, and Geoffrey Hinton. A simple framework for contrastive learning of visual representations. In *International conference on machine learning*, pages 1597–1607. PmlR, 2020.
- [37] Ashish Vaswani, Noam Shazeer, Niki Parmar, Jakob Uszkoreit, Llion Jones, Aidan N Gomez, Łukasz Kaiser, and Illia Polosukhin. Attention is all you need. *Advances in neural information processing systems*, 30, 2017.

- [38] Dominique Makowski, Tam Pham, Zen J. Lau, Jan C. Brammer, François Lespinasse, Hung Pham, Christopher Schölzel, and S. H. Annabel Chen. NeuroKit2: A python toolbox for neurophysiological signal processing. *Behavior Research Methods*, 53(4):1689–1696, feb 2021. doi: 10.3758/s13428-020-01516-y.
- [39] Oliver J Rider, Upasana Tayal, Jane M Francis, Mohammed K Ali, Monique R Robinson, James P Byrne, Kieran Clarke, and Stefan Neubauer. The effect of obesity and weight loss on aortic pulse wave velocity as assessed by magnetic resonance imaging. *Obesity*, 18(12):2311–2316, 2010.
- [40] Michel E Safar, Athanase Protogerou, and Jacques Blacher. Central blood pressure under angiotensin and calcium channel blockade, 2009.
- [41] Eunsoo Moon, Paola Lavin, Kai-Florian Storch, and Outi Linnaranta. Effects of antipsychotics on circadian rhythms in humans: a systematic review and meta-analysis. *Progress in Neuro-Psychopharmacology and Biological Psychiatry*, 108:110162, 2021.
- [42] Carissa Gardiner, Jonathon Weakley, Louise M Burke, Gregory D Roach, Charli Sargent, Nirav Maniar, Minh Huynh, Dean J Miller, Andrew Townshend, and Shona L Halson. The effect of alcohol on subsequent sleep in healthy adults: A systematic review and meta-analysis. *Sleep Medicine Reviews*, 80:102030, 2025.
- [43] Jianlin Su, Murtadha Ahmed, Yu Lu, Shengfeng Pan, Wen Bo, and Yunfeng Liu. Roformer: Enhanced transformer with rotary position embedding. *Neurocomputing*, 568:127063, 2024.
- [44] Sepp Hochreiter and Jürgen Schmidhuber. Long short-term memory. *Neural computation*, 9(8):1735–1780, 1997.
- [45] Kaiming He, Xinlei Chen, Saining Xie, Yanghao Li, Piotr Dollár, and Ross Girshick. Masked autoencoders are scalable vision learners. In *Proceedings of the IEEE/CVF conference on computer vision and pattern recognition*, pages 16000–16009, 2022.

A. Discussion

A.1. Limitations and Future Work

WavesFM has several limitations that point to future directions. First, the model assumes availability of both PPG and ACC channels from a single device type, and was not trained to accommodate missing modalities and may not generalize across heterogeneous hardware devices. Modality-dropout pretraining and cross-device adaptation are promising directions in future work to enable robust performance under missing channels and heterogeneous hardware. Second, the subject-level design targets stable, persistent health conditions and has not been evaluated on tasks requiring finer temporal resolution, such as acute event detection or intra-day physiological dynamics. Finally, the dense subject-level embedding lacks clinical interpretability without offering an account of which signal characteristics drove a given prediction. Future work could address this limitation through post-hoc attribution or disentangled representation learning.

We are committed to the principles of open science and acknowledge the importance of open data in advancing scientific inquiry. We acknowledge that developing and validating our methods on closed, non-public datasets limits the scientific community from fully replicating our work. At the same time, given the sensitive nature of health data, these considerations must be balanced with protecting the privacy of our participants and the security of their personal health information. Although we understand that the inability to release this data constitutes a limitation, we are confident that the findings derived from it provide significant and beneficial insights to the research community.

A.2. Broader Impacts

WavesFM advances research on evaluating meaningful health information from continuous, passively collected wearable data, with several potential societal impacts. By enabling automated health characterization and condition monitoring from consumer-grade devices, the framework could potentially lower barriers to early disease detection and longitudinal health tracking, particularly for populations with limited access to frequent clinical care. Subject-level representations learned from raw waveforms may also accelerate clinical research by providing richer phenotyping tools for observational studies and clinical trials, reducing reliance on costly or invasive assessments.

B. Dataset Details

In this section, we provide details regarding the pretraining and downstream datasets, as well as the associated signal processing pipeline. Across all datasets, we utilize de-identified PPG and ACC waveforms from participants who provided voluntary informed consent for the use of their data in the research and development of novel health and wellness features. Additionally, a secondary research exemption determination was obtained from an Institutional Review Board (IRB).

Stage I pretraining dataset. For Stage I pretraining, the dataset was curated from 324k individuals. For each participant, we intermittently sampled 5k segments of 15s duration, resulting in a corpus of approximately 6.8M hours of recordings (324k individuals \times 5k segments \times 15s). Detailed demographic information for this cohort is provided in Figure 6.

Signal processing. Raw 15s signal segments are extracted for each subject. After computing the one-dimensional magnitude of the three-axis ACC data, both modalities are resampled to $f_s = 100\text{Hz}$ using a polyphase FIR filter (`scipy.signal.resample_poly`). We then apply a standard FIR bandpass filter (`scipy.signal.firwin`), utilizing a passband of 1-12Hz for the PPG signals and 0.5-49.0Hz for the ACC magnitude. Finally, each channel is independently normalized using Z-score

normalization.

Stage II pretraining dataset. The Stage II pretraining dataset consists of a longitudinal subset of the Stage I cohort. Specifically, we selected 10k individuals with at least one week of available data, yielding 61.2k unique week-long recordings and totaling 5.3M hours (47.4% missingness). Demographic information for this subset is detailed in Figure 7.

Downstream dataset. The downstream dataset comprises a held-out cohort of 11,736 participants from the Fitbit Hypertension Study. Data collection was performed under an IRB-approved protocol with informed consent. This dataset includes an average of 11.7 weeks of recordings per subject, alongside 58 self-reported features covering demographics, lifestyle behaviors, health conditions, and medical treatments. We performed a subject-level split into training (70%, $N = 10,988$), validation (15%, $N = 2,356$), and test (15%, $N = 2,356$) sets. The demographic and label distributions for the test set are illustrated in Figure 8 and Figure 9, respectively. Full text of survey questions for demographics, lifestyle, health conditions, and treatment downstream tasks provided to participants are listed in Table 3, Table 4, Table 5, Table 6, respectively.

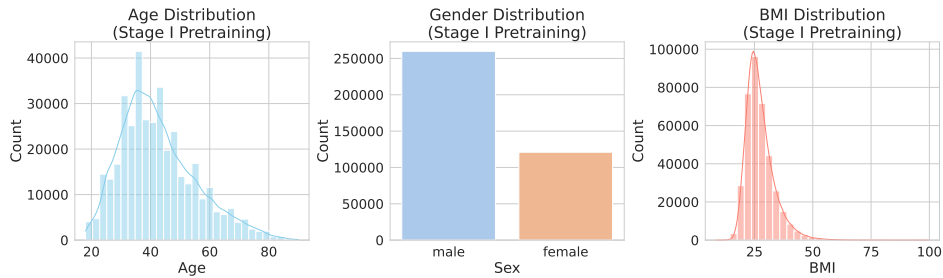


Figure 6 | Cohort demographics (Stage I pretraining dataset).

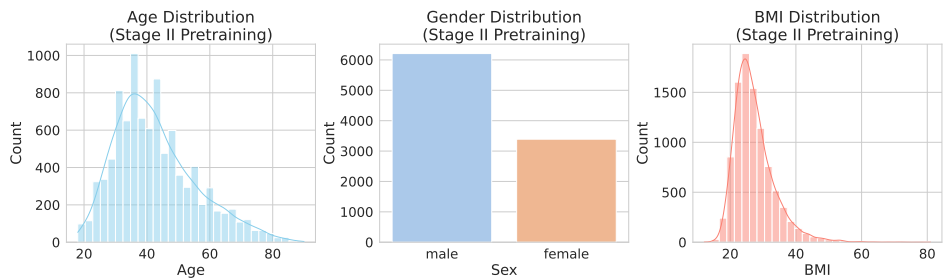


Figure 7 | Cohort demographics (Stage II pretraining dataset).

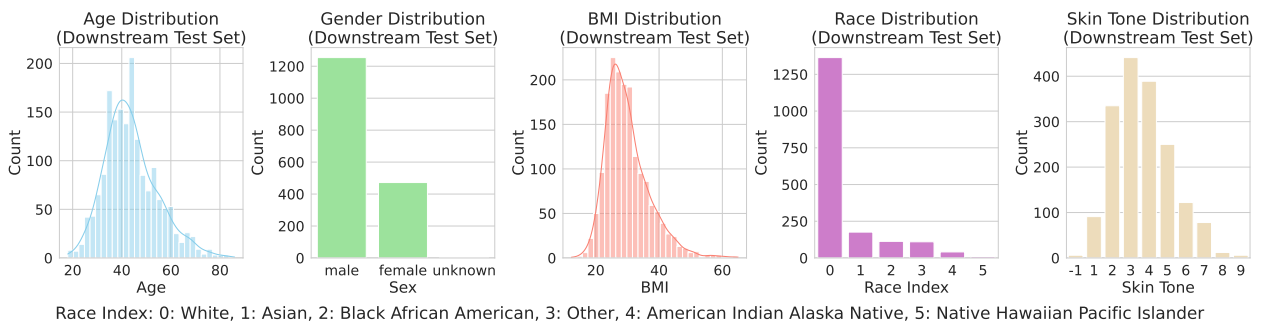


Figure 8 | Cohort demographics (downstream test split).

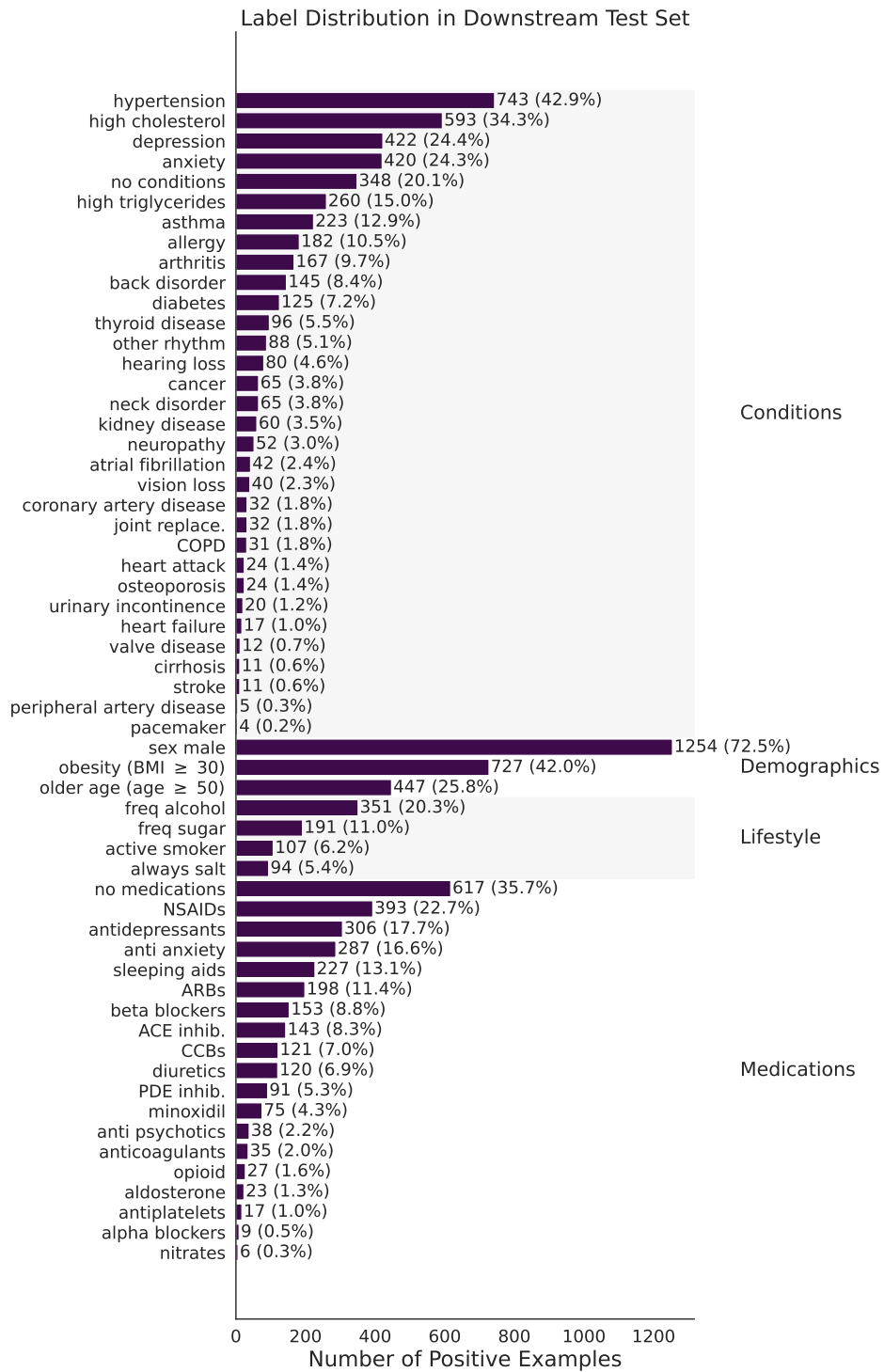


Figure 9 | Label distribution (downstream test split).

Table 3 | Survey Questionnaire: Demographics

Question	Options / Format
What is your date of birth?	Date Picker (e.g., MM/DD/YYYY)
What is your current height?	Text Input (e.g., feet/inches or cm)
What is your current weight?	Text Input (e.g., lbs or kg)
What was your sex assigned at birth?	Male / Female / Other / Prefer not to answer

Table 4 | Survey Questionnaire: Lifestyle

Question	Options
How often did you have a drink containing alcohol in the past year?	Never / Monthly or less / Two to four times a month / Two to three times a week / Four or more times a week / I prefer not to answer
Please select the option that best describes your cigarette (or other tobacco products) use:	Never smoker / Former smoker (quit > 5 years ago) / Former smoker (quit between 1 and 5 years ago) / Former smoker (quit < 1 year ago or currently using inhaled nicotine doses) / Current smoker / Live with an active smoker in home
Do you add salt to your food? (Do not include salt used in cooking)	Never/rarely / Sometimes / Usually / Always / Prefer not to answer
On average, how many glasses, cans, or cartons containing 250 mL of sugar-sweetened beverages, artificially sweetened beverages, or natural juices do you drink per day?	0 / More than 0 to 1 / More than 1 / More than 2 / Prefer not to answer

C. Model and Training Details

C.1. WavesFM Implementation Details

Stage I. For the segment encoder e_ϕ , we employ the EfficientNet-B7 architecture. The input PPG and ACC magnitude segments are treated as $C = 2$ distinct channels, yielding an input shape of $C \times l$, where $l = 15 \text{ s} \times 100 \text{ Hz} = 1500$ time steps. This encoder produces segment embeddings \mathbf{e}_k with a dimensionality of $d = 256$. The projection head g_ω is implemented as a two-layer multi-layer perceptron (MLP) that maps these representations to contrastive projections \mathbf{q}_k of dimensionality $d' = 128$. During model optimization, we performed a hyperparameter sweep over peak learning rates in the range $[1\text{e-}4, 1\text{e-}2]$ and weight decay values in the range $[1\text{e-}6, 1\text{e-}2]$. The final selected configuration utilizes the Adam optimizer with a peak learning rate of $2\text{e-}4$, a linear warmup of 5,000 steps, a weight decay of $1\text{e-}6$, and a total training duration of 2,000,000 steps. The contrastive learning framework is trained with a batch size of 1024 and a temperature parameter $\gamma = 0.04$.

Stage II. The temporal encoder consists of a 6-layer Transformer with a hidden dimension of $d = 256$, an MLP dimension of 768, and 4 attention heads. Both the local and global decoders are configured as 4-layer Transformers with a hidden dimension of 256 and 4 attention heads. The local decoder employs target factorized positional embeddings as queries and the encoder context embeddings as keys and values via cross-attention. Conversely, the global decoder processes the concatenation of the mean-pooled context embedding and the target positional embeddings. The factorized positional embeddings are composed of two learnable lookup tables representing the day of week and time of day, denoted as $\mathbf{P}_{\text{dow}} \in \mathbb{R}^{7 \times D}$ and $\mathbf{P}_{\text{tod}} \in \mathbb{R}^{288 \times D}$, respectively. Each input sequence spans one week, divided into $M = 2016$ five-minute bins, from which a context set of size $N_{\text{ctx}} = 252$ is sampled using a patch size $P \sim \text{Uniform}(\{1, 2, 4\})$. Stage II models are trained for 600,000 iterations with a batch

Table 5 | Survey Questionnaire: Health Conditions Checklist

Question: Have you ever been told by a doctor or other health professional that you have or have had any of the following? (*Check all that apply*)

- | | |
|---|--|
| <ul style="list-style-type: none"> • High blood pressure (hypertension) • Heart attack (myocardial infarction) • Stroke or transient ischemic attack (ministroke) • Atrial Fibrillation (AFib) • Other heart rhythm problem (arrhythmia) • Heart failure (or congestive heart failure) • Coronary artery disease or angina • Peripheral artery disease • Heart valve disease • A pacemaker or an implantable defibrillator (ICD) • Diabetes • High cholesterol • High triglycerides • Arthritis • Hip or knee replacement • Low back disorder / chronic back defect | <ul style="list-style-type: none"> • Neck disorder / chronic neck defect • Osteoporosis • Asthma • Chronic bronchitis, COPD, or emphysema • Rhinitis, hay fever, allergies (excl. asthma) • Kidney problems • Thyroid disease • Cancer • Cirrhosis of the liver • Urinary incontinence • Neuropathy • Depression • Anxiety disorder • Hearing loss • Vision loss • None of the above |
|---|--|

Table 6 | Survey Questionnaire: Medications Taken in the Past 30 Days

Question: Please check any of the following medications you have taken in the *past 30 days*. (*Note: Examples are provided for each medication class, but are not comprehensive.*)

Medication Class	Examples / Specifics
ACE inhibitors	Lisinopril (Zestril, Prinivil), Enalapril (Vasotec), Ramipril (Altace)
Angiotensin Receptor Blockers	Losartan (Cozaar), Valsartan (Diovan), Candesartan (Atacand)
Diuretics	Hydrochlorothiazide (HCTZ) (Microzide), Furosemide (Lasix), Chlorthalidone (Hygroton)
Beta blockers	Metoprolol (Lopressor, Toprol XL), Carvedilol (Coreg), Atenolol (Tenormin)
Calcium channel blockers	Amlodipine (Norvasc), Diltiazem (Cardizem), Verapamil (Calan, Isoptin)
Aldosterone antagonists	Spirolactone (Aldactone), Eplerenone (Inspra)
Minoxidil	Rogaine
Nitrates	Nitroglycerin (Nitrostat, Nitro-Bid), Isosorbide mononitrate (Imdur), Isosorbide dinitrate (Isordil)
Phosphodiesterase inhibitors	Sildenafil (Viagra, Revatio), Tadalafil (Cialis, Adcirca), Vardenafil (Levitra, Staxyn)
Alpha-blockers	Doxazosin (Cardura), Prazosin (Minipress), Terazosin (Hytrin)
Other Classes (<i>No examples given</i>)	Anti-anxiety aids, Anti-psychotics, Anticoagulants, Antidepressants, Antiplatelets, Certain types of chemotherapy, Opioid painkillers, NSAIDs, Sleeping aids, or None of the above

size of 32 using the Adam optimizer and a cosine decay learning rate schedule, including a linear warmup for the first 1/8 of the iterations (75k steps). While the peak learning rate was searched over the candidate set $\{1e-4, 4e-4, 8e-4\}$, a final learning rate of $8e-4$ was selected.

Compute resources. The Stage I segment encoder training was distributed across a cluster equivalent to an NVIDIA DGX-2 system ($16 \times V100$ GPUs), with each training run concluding in approximately

96 hours. The Stage II temporal encoder was optimized using hardware equivalent to an NVIDIA V100 GPU, with each training run requiring approximately 24 hours to complete.

C.2. Behavior-Centric Baseline Implementation Details

To construct a directly comparable behavior-centric baseline, we extract a comprehensive suite of 19 expert-crafted physiological and kinematic features from the synchronized PPG and ACC signals. Given the raw segments of shape $C \times l = 4 \times 1500$, we compute 10 PPG-derived cardiac metrics and 9 ACC-derived kinematic metrics.

The mathematical formulation and physical descriptions of these 19 features are cataloged in Table 7. For the cardiac stream, signal cleaning, peak detection, and standard heart rate variability (HRV) metrics are implemented using the NeuroKit2 (<https://pypi.org/project/neurokit2/>) library. For the kinematic stream, metrics are designed to capture signal energy, spatial orientation, and movement dynamics.

Table 7 | Overview of 19 expert-crafted PPG and ACC features.

Source	Feature Name	Mathematical Description
PPG	Heart_Rate_BPM_Mean	Mean heart rate computed across the 15 s window in beats per minute.
	RR_Mean_Msec	Mean interval between successive normal cardiac cycles (NN).
	RR_Median_Msec	Median interval of the NN sequence.
	RR_20th_Percentile_Msec	20th percentile value of the NN interval distribution.
	RR_80th_Percentile_Msec	80th percentile value of the NN interval distribution.
	RMSSD_Msec	Root mean square of successive differences between adjacent NN intervals.
	SDNN_Msec	Standard deviation of the NN intervals.
	Shannon_Ent_RR_Nats	Shannon entropy evaluated over the distribution of NN intervals.
	Shannon_Ent_RR_Diffs_Nats	Shannon entropy of the differences between successive NN intervals.
	PNN30_Percent	Percentage of successive NN intervals that differ by more than 30 ms.
ACC	Log_Energy	Logarithm of the sum of the root-mean-square values across the three axes.
	Log_Energy_Ratio	Logarithm of the ratio of energy in the first Principal Component (PC ₁) to the total 3-axis root-mean-square magnitude energy.
	Jerk_Autocorr_Ratio	Average lag-1 autocorrelation of the kinematic jerk, normalized by the energy of PC ₁ .
	Covariance_Condition	Matrix condition number of the 3 × 3 tri-axial acceleration covariance matrix.
	Zero_Crossing_Avg_Seconds	Mean duration between sequential zero-crossings of the PC ₁ timeseries.
	Zero_Crossing_Std_Seconds	Standard deviation of durations between zero-crossings of the PC ₁ timeseries.
	Robust_Arm_Tilt	Logarithm of the mean root-sum-of-squares of the lateral (X) and vertical (Z) axes.
	Kurtosis	Kurtosis of the 3-axis root-mean-square acceleration magnitude.
Sleep_Coefficient	Digitized integer assignment of the cumulative peak-to-peak range binned across 16 log-spaced thresholds.	

To transform these local features into longitudinal trajectories suitable for temporal modeling, the statistical features extracted from individual windows are aggregated and averaged over 5-minute resolutions. For a full week-long recording, this mapping converts the underlying high-frequency waveforms into a feature matrix of shape 2016×19 , where 2016 represents the number of 5-minute steps in a 7-day epoch, and 19 represents the distinct feature dimensionality.

Prior to model ingestion, we apply independent per-feature standardization (Z-score scaling) across the feature dimensions. This normalized sequence is then passed directly into a Stage II temporal

encoder. To ensure a comparable evaluation of representation learning performance, this baseline utilizes an identical architecture configuration (6-layer Transformer, 4 attention heads, $d = 256$ hidden state dimensionality) and the exact same hyperparameter schedule detailed in Appendix C.1.

C.3. Supervised Learning Baselines Implementation

To contextualize the performance of our self-supervised temporal encoder, we implement a suite of supervised sequence architectures trained directly on the downstream labeled data. For each baseline approach, a standalone sequential model is optimized end-to-end to process the longitudinal sequence of segment embeddings (of shape $M \times d = 2016 \times 256$) and map it directly to the target health label.

- **Weighted Pooling:** This architecture maps inputs through an initial `LayerNorm` block before passing each segment embedding $\mathbf{v}_t \in \mathbb{R}^d$ through a linear gating function $G : \mathbb{R}^d \rightarrow \mathbb{R}$ to compute an unnormalized scalar importance score s_t . To handle missingness and irregular sampling gaps, padded elements are masked out by forcing their scores to $-\infty$. The sequence scores are normalized via a softmax operation to yield temporal weights, $\alpha_t = \exp(s_t) / \sum_{j=1}^M \exp(s_j)$, which are used to compress the sequence into a static representation, $\bar{\mathbf{v}} = \sum_{t=1}^M \alpha_t \mathbf{v}_t$. This pooled context vector is passed through a dropout layer ($\rho = 0.2$) and evaluated by a final linear dense projection head.
- **Cross-Attention:** This model computes directed interactions between a learnable classification token ($\mathbf{q}_{\text{CLS}} \in \mathbb{R}^d$) and the sequence context. The CLS token serves as the query (**Q**), while the normalized longitudinal embeddings function as keys (**K**) and values (**V**). Absolute positional relationships are preserved by factoring a Rotary Positional Embedding (RoPE) [43] directly into the query and key heads based on their actual index positions (with the query evaluated at position 0). An asymmetric boolean mask restricts the query token from attending to invalid or missing context intervals. The updated classification embedding is routed through a standard two-layer Multi-Layer Perceptron (MLP) block utilizing a GELU activation layer and dropout ($\rho = 0.2$) before emitting the final projection logits.
- **LSTM:** This model captures long-term autoregressive dependencies using a recurrent Long Short-Term Memory network [44] configured with a hidden dimensionality of 64. To prevent invalid intervals or missing segments from corrupting the forward memory cell parameters, the model evaluates an element-wise conditional check; if a step fails the missingness check, the cell update step propagates the un-modified hidden state (\mathbf{h}_{t-1}) and cell state (\mathbf{c}_{t-1}) directly into the subsequent window step. The terminal hidden state (\mathbf{h}_M) is filtered through a dropout layer ($\rho = 0.2$) and processed by a dense linear projection head to yield the final classification logit.

C.4. Evaluating Open-Source PPG Foundation Models

To assess the representation capability of our foundation model, we benchmark downstream performance against a collection of open-source and pretrained PPG foundation models. These models represent the latest state-of-the-art in self-supervised and cross-modal pretraining for PPG, providing critical reference points to evaluate generalizability. Specifically, we include PaPaGei [11], Pulse-PPG [12], and AnyPPG [13] in our comparative analysis.

The details of these three state-of-the-art baselines are detailed as follows:

- **PaPaGei:** this model utilizes a ResNet optimized through a morphology-aware framework that pairs signals with similar blood volume dynamics across different participants and simultaneously trains multiple expert heads to predict key physiological pulse shape metrics. The encoder processes 10s segments sampled at 125Hz, producing a static representation vector of dimensionality $d = 512$ per segment.

- **Pulse-PPG:** Pulse-PPG utilizes a 1D ResNet-26 backbone optimized via a motif-based relative contrastive learning framework, explicitly mapping the non-linear distances between waveform segments. The model captures long-term contextual patterns over 4-minute window inputs resampled at 50Hz, ultimately transforming each signal segment into a vector of dimensionality $d = 512$.
- **AnyPPG:** AnyPPG shifts the unimodal paradigm by executing a cross-modal, dual-branch pretraining objective where a 1D ResNet PPG encoder is guided symmetrically via text-image alignment metrics alongside a frozen ECGF_{ounder} cross-modal backbone. Trained over a heterogeneous multi-source corpus, the PPG branch evaluates filtered 10s signal slices at 125 Hz to map localized cardiovascular dynamics directly into a final embedding space of dimensionality $d = 512$.

To ensure a fair comparison, raw PPG waveforms are independently preprocessed, resampled, and structurally framed to match the input settings specified by each respective open-source baseline. For each isolated segment extracted from a given dataset, we retrieve the corresponding frozen embedding vector ($d = 512$ for all three models). These segment-level representations are subsequently averaged across the temporal domain at the subject level to derive a single subject-specific representation vector, which is then utilized to train and evaluate downstream linear probes.

D. Detailed Results

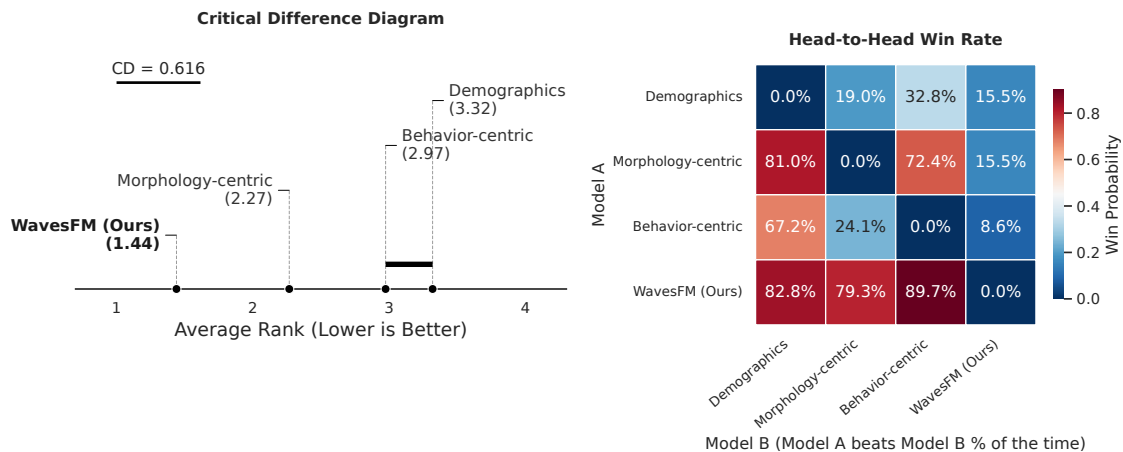


Figure 10 | **Statistical evaluation across 58 benchmark tasks.** (Left) Critical Difference diagram based on post-hoc Nemenyi test ($\alpha = 0.05$, $CD = 0.616$). WavesFM achieves a significantly better average rank (1.44) than all baselines; thick horizontal bars indicate no statistically significant difference ($p \geq 0.05$). (Right) Pairwise win rate matrix showing the percentage of tasks where Model A yields a superior AUROC over Model B. WavesFM demonstrates robust multi-task performance.

D.1. Comparison with Morphology- and Behavior-Centric Baselines

In Table 8, we present the comprehensive performance metrics across all classification tasks. All reported metrics include 95% confidence intervals derived from 1000 test-set bootstrap iterations. Additionally, we provide the mean AUC and pAUC aggregated by category, alongside the overall mean across all tasks. WavesFM achieves the highest performance on the majority of tasks, with the best results highlighted in bold.

We systematically evaluate the generalization capabilities of our framework across the complete 58-task benchmark suite. The Critical Difference diagram (Figure 10) shows that WavesFM achieved the top average rank (1.44) and is statistically distinct from all baselines. This robust generalization is further emphasized by the head-to-head win matrix.

Table 8 | Detailed Results for Downstream Tasks. CCB: calcium channel blocker; ARB: angiotension receptor blocker; PDE: phosphodiesterase; ACE: angiotension-converting enzyme; NSAID: nonsteroidal anti-inflammatory drugs; PAD: peripheral artery disease; CAD: coronary artery disease; AFib: atrial fibrillation; COPD: chronic obstructive pulmonary disease

Task	Demographics		Behavior-Centric		Morphology-Centric		WavesFM	
	AUROC [†]	pAUC [†]	AUROC [†]	pAUC [†]	AUROC [†]	pAUC [†]	AUROC [†]	pAUC [†]
Demographics								
sex male	1.000 [1.000, 1.000]	1.000 [1.000, 1.000]	0.975 [0.968, 0.981]	0.913 [0.889, 0.938]	0.993 [0.988, 0.996]	0.971 [0.947, 0.986]	0.996 [0.992, 0.998]	0.983 [0.962, 0.994]
older age (age ≥ 50)	1.000 [1.000, 1.000]	1.000 [1.000, 1.000]	0.881 [0.863, 0.897]	0.724 [0.697, 0.750]	0.945 [0.934, 0.955]	0.824 [0.799, 0.853]	0.959 [0.950, 0.968]	0.852 [0.829, 0.877]
obesity (BMI ≥ 30)	1.000 [1.000, 1.000]	1.000 [1.000, 1.000]	0.817 [0.796, 0.837]	0.663 [0.641, 0.688]	0.921 [0.908, 0.933]	0.798 [0.773, 0.824]	0.928 [0.917, 0.940]	0.814 [0.790, 0.837]
Mean (Demographics)	1.000 ± 0.000	1.000 ± 0.000	0.891 ± 0.079	0.767 ± 0.131	0.953 ± 0.037	0.864 ± 0.093	0.961 ± 0.034	0.883 ± 0.089
Lifestyle								
freq sugar	0.583 [0.554, 0.611]	0.512 [0.501, 0.525]	0.694 [0.654, 0.733]	0.556 [0.533, 0.583]	0.688 [0.650, 0.726]	0.559 [0.535, 0.584]	0.697 [0.658, 0.736]	0.561 [0.538, 0.587]
always salt	0.613 [0.566, 0.660]	0.524 [0.502, 0.549]	0.598 [0.540, 0.655]	0.514 [0.491, 0.541]	0.598 [0.540, 0.652]	0.520 [0.496, 0.546]	0.605 [0.545, 0.660]	0.524 [0.499, 0.550]
active smoker	0.612 [0.568, 0.654]	0.525 [0.503, 0.548]	0.722 [0.664, 0.776]	0.580 [0.546, 0.616]	0.736 [0.686, 0.787]	0.603 [0.569, 0.639]	0.784 [0.734, 0.830]	0.635 [0.596, 0.677]
freq alcohol	0.583 [0.541, 0.623]	0.539 [0.521, 0.560]	0.743 [0.714, 0.774]	0.583 [0.561, 0.608]	0.661 [0.630, 0.692]	0.540 [0.523, 0.559]	0.833 [0.808, 0.857]	0.672 [0.642, 0.703]
Mean (Lifestyle)	0.598 ± 0.017	0.525 ± 0.011	0.689 ± 0.064	0.558 ± 0.032	0.671 ± 0.058	0.555 ± 0.036	0.730 ± 0.100	0.598 ± 0.068
Treatment								
nitrates	0.756 [0.620, 0.860]	0.499 [0.474, 0.562]	0.805 [0.692, 0.913]	0.559 [0.474, 0.735]	0.811 [0.683, 0.928]	0.577 [0.474, 0.717]	0.864 [0.770, 0.940]	0.596 [0.474, 0.746]
antiplatelets	0.735 [0.607, 0.871]	0.658 [0.551, 0.748]	0.816 [0.701, 0.910]	0.678 [0.570, 0.783]	0.833 [0.717, 0.940]	0.731 [0.621, 0.849]	0.846 [0.743, 0.937]	0.719 [0.606, 0.834]
diuretics	0.753 [0.710, 0.790]	0.579 [0.549, 0.603]	0.579 [0.549, 0.603]	0.727 [0.678, 0.771]	0.570 [0.538, 0.602]	0.778 [0.738, 0.817]	0.808 [0.749, 0.828]	0.607 [0.573, 0.643]
CCBs	0.703 [0.660, 0.742]	0.561 [0.534, 0.588]	0.691 [0.643, 0.740]	0.564 [0.533, 0.596]	0.779 [0.731, 0.824]	0.640 [0.601, 0.684]	0.801 [0.756, 0.843]	0.664 [0.625, 0.708]
anticoagulants	0.710 [0.633, 0.775]	0.558 [0.513, 0.605]	0.770 [0.673, 0.854]	0.614 [0.551, 0.680]	0.778 [0.693, 0.852]	0.620 [0.559, 0.683]	0.772 [0.683, 0.850]	0.617 [0.557, 0.680]
beta blockers	0.667 [0.627, 0.706]	0.551 [0.527, 0.572]	0.752 [0.708, 0.791]	0.616 [0.582, 0.650]	0.781 [0.737, 0.818]	0.637 [0.601, 0.671]	0.807 [0.763, 0.846]	0.664 [0.627, 0.700]
ARBs	0.728 [0.697, 0.758]	0.560 [0.538, 0.583]	0.676 [0.637, 0.715]	0.551 [0.527, 0.577]	0.737 [0.702, 0.771]	0.580 [0.553, 0.608]	0.753 [0.719, 0.785]	0.589 [0.562, 0.618]
PDE inhib.	0.744 [0.708, 0.778]	0.537 [0.513, 0.565]	0.716 [0.659, 0.770]	0.561 [0.527, 0.596]	0.735 [0.691, 0.777]	0.546 [0.516, 0.578]	0.731 [0.686, 0.775]	0.548 [0.517, 0.585]
ACE inhib.	0.723 [0.687, 0.757]	0.558 [0.535, 0.582]	0.690 [0.644, 0.732]	0.540 [0.515, 0.566]	0.727 [0.687, 0.766]	0.567 [0.539, 0.600]	0.723 [0.686, 0.762]	0.571 [0.543, 0.605]
aldosterone	0.666 [0.568, 0.757]	0.508 [0.474, 0.549]	0.738 [0.623, 0.834]	0.559 [0.503, 0.621]	0.762 [0.651, 0.851]	0.587 [0.521, 0.658]	0.729 [0.622, 0.813]	0.543 [0.490, 0.604]
alpha blockers	0.642 [0.504, 0.754]	0.474 [0.474, 0.475]	0.702 [0.521, 0.826]	0.474 [0.474, 0.477]	0.666 [0.521, 0.796]	0.477 [0.474, 0.494]	0.710 [0.536, 0.860]	0.483 [0.474, 0.513]
minoxidil	0.652 [0.597, 0.703]	0.529 [0.505, 0.556]	0.629 [0.568, 0.691]	0.536 [0.505, 0.568]	0.663 [0.598, 0.725]	0.541 [0.512, 0.576]	0.687 [0.627, 0.747]	0.565 [0.529, 0.607]
opioid	0.631 [0.536, 0.711]	0.529 [0.498, 0.567]	0.786 [0.683, 0.881]	0.660 [0.586, 0.733]	0.785 [0.683, 0.888]	0.719 [0.638, 0.805]	0.831 [0.727, 0.916]	0.749 [0.656, 0.839]
NSAIDs	0.580 [0.553, 0.607]	0.517 [0.505, 0.529]	0.581 [0.549, 0.612]	0.519 [0.506, 0.534]	0.619 [0.589, 0.650]	0.520 [0.506, 0.534]	0.615 [0.585, 0.648]	0.520 [0.506, 0.536]
antidepressants	0.611 [0.581, 0.642]	0.531 [0.516, 0.547]	0.741 [0.710, 0.771]	0.595 [0.572, 0.621]	0.771 [0.742, 0.798]	0.617 [0.591, 0.642]	0.819 [0.793, 0.846]	0.664 [0.634, 0.695]
anti psychotics	0.577 [0.507, 0.638]	0.507 [0.483, 0.538]	0.790 [0.703, 0.869]	0.658 [0.593, 0.724]	0.752 [0.670, 0.827]	0.602 [0.548, 0.660]	0.828 [0.751, 0.898]	0.681 [0.618, 0.750]
anti anxiety	0.615 [0.584, 0.645]	0.530 [0.517, 0.548]	0.721 [0.687, 0.752]	0.576 [0.551, 0.601]	0.724 [0.692, 0.754]	0.571 [0.547, 0.595]	0.757 [0.724, 0.787]	0.604 [0.580, 0.633]
sleeping aids	0.563 [0.531, 0.599]	0.513 [0.500, 0.529]	0.634 [0.592, 0.673]	0.535 [0.517, 0.555]	0.605 [0.567, 0.645]	0.531 [0.512, 0.553]	0.642 [0.604, 0.683]	0.549 [0.527, 0.572]
none	0.624 [0.601, 0.648]	0.531 [0.519, 0.545]	0.669 [0.644, 0.694]	0.542 [0.526, 0.558]	0.710 [0.688, 0.735]	0.553 [0.537, 0.575]	0.720 [0.697, 0.743]	0.549 [0.532, 0.571]
Mean (Treatment)	0.667 ± 0.063	0.538 ± 0.039	0.718 ± 0.063	0.574 ± 0.052	0.738 ± 0.062	0.590 ± 0.063	0.759 ± 0.068	0.604 ± 0.070
Health Conditions								
cancer	0.741 [0.682, 0.792]	0.594 [0.550, 0.633]	0.673 [0.596, 0.741]	0.574 [0.530, 0.622]	0.708 [0.638, 0.773]	0.574 [0.531, 0.619]	0.718 [0.651, 0.781]	0.583 [0.540, 0.626]
PAD	0.902 [0.785, 0.974]	0.709 [0.534, 0.864]	0.973 [0.923, 0.998]	0.870 [0.645, 0.991]	0.977 [0.929, 1.000]	0.887 [0.648, 1.000]	0.968 [0.899, 1.000]	0.884 [0.647, 1.000]
pacemaker	0.710 [0.544, 0.895]	0.547 [0.474, 0.726]	0.935 [0.885, 0.999]	0.676 [0.474, 0.995]	0.925 [0.738, 1.000]	0.843 [0.474, 1.000]	0.969 [0.913, 1.000]	0.837 [0.547, 1.000]
CAD	0.821 [0.768, 0.868]	0.613 [0.560, 0.674]	0.830 [0.750, 0.901]	0.671 [0.601, 0.746]	0.866 [0.796, 0.924]	0.688 [0.610, 0.771]	0.871 [0.811, 0.923]	0.816 [0.607, 0.770]
heart failure	0.771 [0.681, 0.862]	0.574 [0.509, 0.651]	0.797 [0.637, 0.909]	0.625 [0.531, 0.713]	0.832 [0.711, 0.941]	0.712 [0.598, 0.827]	0.882 [0.808, 0.949]	0.712 [0.611, 0.835]
AFib	0.813 [0.761, 0.864]	0.630 [0.579, 0.683]	0.791 [0.720, 0.861]	0.624 [0.564, 0.693]	0.823 [0.754, 0.887]	0.658 [0.597, 0.721]	0.823 [0.753, 0.887]	0.664 [0.600, 0.730]
heart attack	0.744 [0.654, 0.828]	0.595 [0.534, 0.661]	0.832 [0.753, 0.900]	0.639 [0.558, 0.727]	0.852 [0.765, 0.925]	0.677 [0.595, 0.766]	0.860 [0.781, 0.930]	0.669 [0.584, 0.767]
hypertension	0.689 [0.668, 0.711]	0.559 [0.544, 0.573]	0.694 [0.668, 0.720]	0.560 [0.542, 0.581]	0.734 [0.711, 0.758]	0.594 [0.576, 0.613]	0.739 [0.717, 0.763]	0.597 [0.578, 0.618]
stroke	0.599 [0.445, 0.752]	0.606 [0.515, 0.708]	0.623 [0.460, 0.780]	0.512 [0.474, 0.605]	0.667 [0.491, 0.829]	0.542 [0.474, 0.659]	0.736 [0.582, 0.878]	0.602 [0.501, 0.725]
other rhythm	0.591 [0.542, 0.643]	0.504 [0.487, 0.523]	0.674 [0.616, 0.728]	0.535 [0.506, 0.570]	0.636 [0.574, 0.695]	0.535 [0.506, 0.568]	0.660 [0.601, 0.715]	0.539 [0.510, 0.574]
valve disease	0.551 [0.426, 0.713]	0.513 [0.474, 0.575]	0.615 [0.406, 0.819]	0.573 [0.489, 0.677]	0.671 [0.510, 0.816]	0.541 [0.474, 0.661]	0.643 [0.485, 0.798]	0.529 [0.474, 0.635]
cirrhosis	0.607 [0.444, 0.765]	0.559 [0.492, 0.640]	0.637 [0.472, 0.801]	0.557 [0.474, 0.672]	0.725 [0.590, 0.856]	0.592 [0.474, 0.720]	0.689 [0.557, 0.832]	0.607 [0.474, 0.754]
anxiety	0.680 [0.656, 0.705]	0.571 [0.553, 0.592]	0.756 [0.731, 0.781]	0.599 [0.574, 0.625]	0.763 [0.737, 0.788]	0.601 [0.579, 0.624]	0.790 [0.765, 0.814]	0.635 [0.612, 0.662]
depression	0.657 [0.631, 0.681]	0.552 [0.537, 0.570]	0.726 [0.697, 0.755]	0.591 [0.570, 0.614]	0.746 [0.719, 0.771]	0.598 [0.577, 0.622]	0.771 [0.745, 0.797]	0.624 [0.601, 0.651]
diabetes	0.738 [0.699, 0.773]	0.575 [0.548, 0.602]	0.796 [0.755, 0.836]	0.631 [0.595, 0.670]	0.816 [0.776, 0.852]	0.656 [0.615, 0.695]	0.836 [0.796, 0.876]	0.691 [0.649, 0.731]
thyroid disease	0.720 [0.675, 0.767]	0.593 [0.563, 0.626]	0.710 [0.654, 0.762]	0.551 [0.522, 0.586]	0.719 [0.665, 0.769]	0.556 [0.524, 0.593]	0.722 [0.667, 0.773]	0.560 [0.528, 0.595]
high cholesterol	0.631 [0.607, 0.654]	0.537 [0.524, 0.551]	0.614 [0.586, 0.640]	0.530 [0.516, 0.546]	0.640 [0.613, 0.664]	0.525 [0.511, 0.540]	0.647 [0.620, 0.672]	0.533 [0.519, 0.548]
high triglycerides	0.598 [0.572, 0.630]	0.504 [0.494, 0.516]	0.620 [0.585, 0.656]	0.526 [0.509, 0.545]	0.607 [0.568, 0.640]	0.521 [0.504, 0.540]	0.625 [0.589, 0.657]	0.525 [0.508, 0.542]
joint replace.	0.831 [0.765, 0.884]	0.641 [0.582, 0.701]	0.810 [0.747, 0.874]	0.636 [0.567, 0.713]	0.866 [0.813, 0.913]	0.655 [0.584, 0.724]	0.866 [0.810, 0.915]	0.664 [0.594, 0.738]
arthritis	0.758 [0.726, 0.788]	0.585 [0.561, 0.613]	0.763 [0.722, 0.798]	0.590 [0.561, 0.620]	0.795 [0.762, 0.826]	0.607 [0.576, 0.639]	0.802 [0.770, 0.831]	0.608 [0.576, 0.642]
osteoporosis	0.804 [0.706, 0.882]	0.701 [0.627, 0.773]	0.767 [0.656, 0.865]	0.615 [0.532, 0.698]	0.763 [0.637, 0.869]	0.660 [0.568, 0.749]	0.767 [0.636, 0.877]	0.651 [0.561, 0.740]
neck disorder	0.672 [0.614, 0.728]	0.535 [0.509, 0.567]	0.649 [0.578, 0.716]	0.544 [0.507, 0.586]	0.699 [0.628, 0.762]	0.572 [0.529, 0.615]	0.705 [0.638, 0.766]	0.576 [0.532, 0.622]
back disorder	0.634 [0.596, 0.673]	0.522 [0.504, 0.540]	0.670 [0.622, 0.712]	0.548 [0.523, 0.574]	0.687 [0.641, 0.733]	0.558 [0.531, 0.587]	0.703 [0.658, 0.750]	0.576 [0.547, 0.609]
neuropathy	0.697 [0.637, 0.749]	0.539 [0.505, 0.566]	0.726 [0.646, 0.802]	0.584 [0.537, 0.635]	0.770 [0.695, 0.837]	0.646 [0.588, 0.706]	0.770 [0.696, 0.840]	0.653 [0.590, 0.715]
kidney disease	0.620 [0.563, 0.691]	0.548 [0.511, 0.578]	0.644 [0.558, 0.723]	0.574 [0.533, 0.620]	0.644 [0.561, 0.725]	0.580 [0.538, 0.634]	0.688 [0.611, 0.759]	0.591 [0.545, 0.644]
COPD	0.596 [0.490, 0.696]	0.518 [0.483, 0.560]	0.749 [0.676, 0.813]	0.539 [0.493, 0.587]	0.704 [0.607, 0.799]	0.558 [0.504, 0.623]	0.733 [0.634, 0	

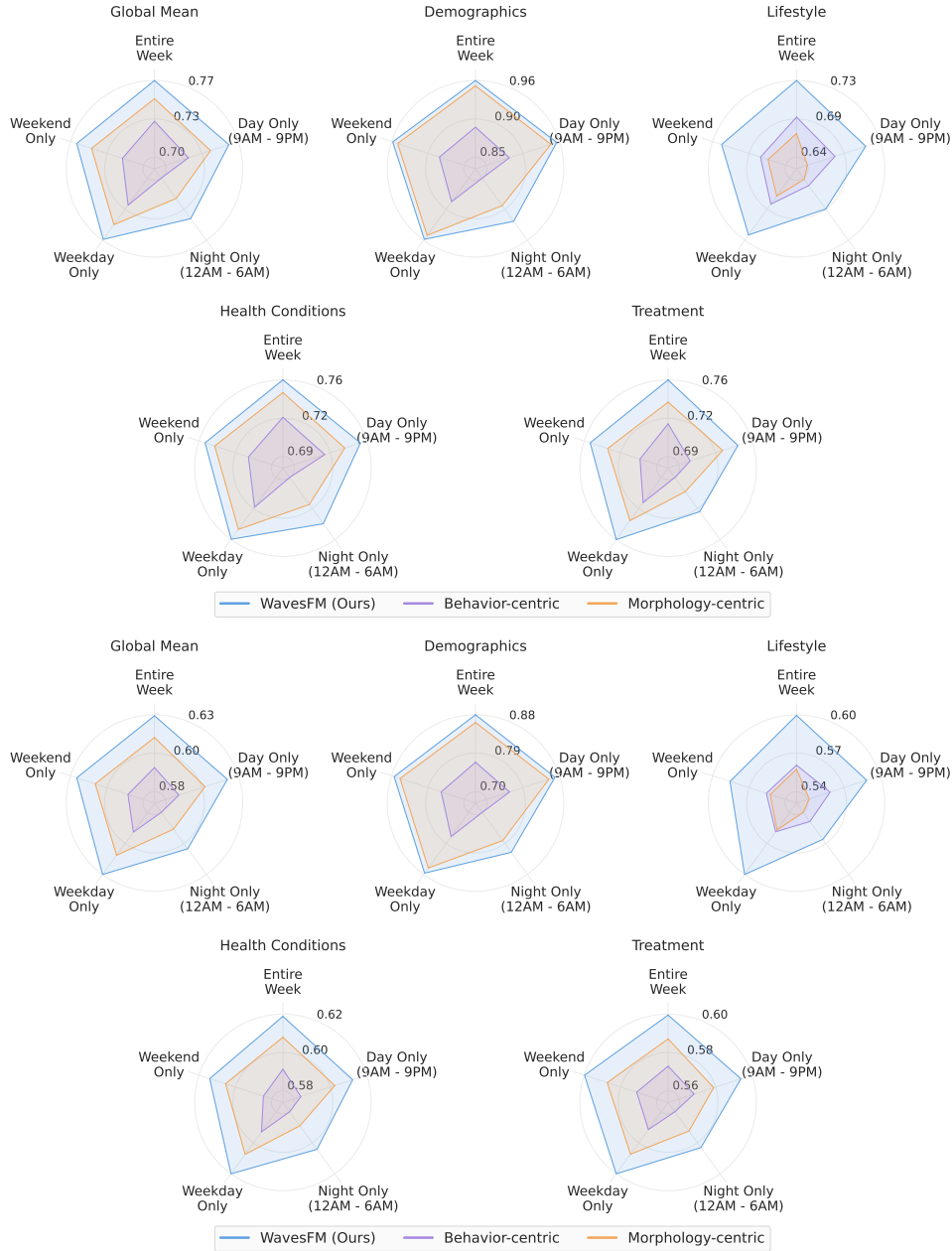


Figure 11 | **Robustness to systematic missingness.** Comparison of WavesFM against morphology- and behavior-centric baselines demonstrates its superior robustness across various missingness scenarios common in wearable data (e.g., weekday-only recording, night-only recording, etc.), evaluated using AUROC (top) and pAUROC (bottom).

D.2. Experiments on Longitudinal Missiness

In Figure 11, we visualize the complete AUC and pAUC performance metrics for the systematic longitudinal missingness experiments, detailing results across all four task categories alongside overall performance. Generally, both WavesFM and the morphology-centric baseline demonstrate fair robustness to missing data, except during nighttime periods where both models experience a performance drop. The behavior-centric baseline, in addition to yielding lower initial performance on the full dataset, exhibits a much more significant drop during nighttime and weekend periods, particularly on health condition (4.7% drop vs 2.3% for WavesFM at night) and treatment tasks (1.9% drop vs 0.8% for WavesFM on weekends). Conversely, an opposite trend emerges in lifestyle tasks,

where the behavior-centric baseline shows greater robustness than the morphology-centric baseline when restricted to strictly daytime (1.8% vs 6.4% drop) or nighttime data (5.0% vs 6.2% drop), although both still underperform WavesFM.

D.3. Comparison with Supervised Baselines

Table 9 presents the classification performance of WavesFM using linear probing compared against three fully supervised baselines (see Appendix C.3 for implementation details on supervised baselines), with all models trained on a restricted 10% subset of the labeled training data. Note that three tasks were excluded from this analysis due to an insufficient prevalence of positive labels in the reduced training set. Overall, WavesFM significantly outperforms the supervised baselines on over 80% of the tasks (45 out of 55), achieving an average AUC improvement of 7.8% over the closest baseline.

D.4. Comparison with Public PPG Foundation Models

In Figure 12, we show detailed comparisons between WavesFM and three other public foundation models under an identical linear probing setup, restricting all models to 10% downstream training split due to long inference time. The corresponding numerical results are provided in Table 10. With nearly all markers falling above the diagonal in these visualizations (49 out of 55 tasks), we can clearly observe WavesFM’s consistent advantage. The only notable exceptions are antiplatelets and valve disease, potentially due to the expected variance associated with small positive sample sizes in the restricted training set ($N = 9$ and $N = 12$, respectively).

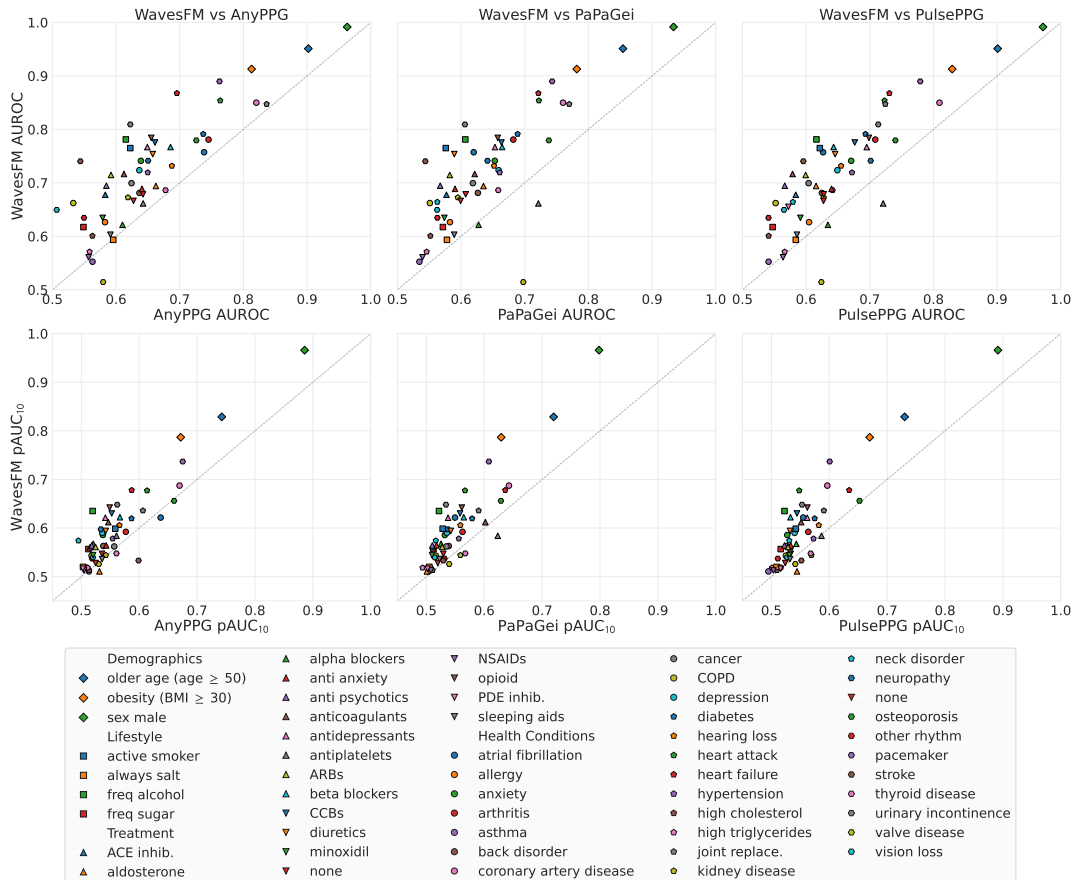


Figure 12 | Performance comparison with Foundation Model Baselines.

Table 9 | Supervised Baseline vs. WavesFM Comparison Results.

Task	# Pos	Cross Attention		LSTM		Weighted Pooling		WavesFM	
		AUROC [†]	pAUC [†]	AUROC [†]	pAUC [†]	AUROC [†]	pAUC [†]	AUROC [†]	pAUC [†]
<i>Demographics</i>									
obesity (BMI \geq 30)	727	0.889	0.751	0.878	0.746	0.822	0.669	0.913	0.787
older age (age \geq 50)	447	0.932	0.805	0.929	0.785	0.919	0.760	0.951	0.829
sex male	1254	0.991	0.965	0.988	0.957	0.952	0.859	0.992	0.966
Mean (Demographics)	—	0.937	0.840	0.932	0.829	0.898	0.763	0.952	0.860
<i>Lifestyle</i>									
active smoker	107	0.696	0.557	0.668	0.520	0.646	0.540	0.765	0.599
always salt	94	0.606	0.505	0.555	0.500	0.580	0.509	0.593	0.520
freq alcohol	351	0.672	0.550	0.604	0.525	0.615	0.517	0.781	0.635
freq sugar	191	0.593	0.541	0.573	0.539	0.566	0.521	0.617	0.557
Mean (Lifestyle)	—	0.642	0.538	0.600	0.521	0.602	0.522	0.689	0.578
<i>Treatment</i>									
ACE inhib.	143	0.678	0.535	0.649	0.543	0.644	0.532	0.678	0.560
ARBs	198	0.688	0.537	0.712	0.559	0.691	0.550	0.715	0.561
CCBs	121	0.675	0.550	0.690	0.557	0.644	0.547	0.775	0.630
NSAIDs	393	0.577	0.515	0.552	0.508	0.560	0.517	0.561	0.513
PDE inhib.	91	0.655	0.513	0.634	0.517	0.577	0.513	0.655	0.516
aldosterone	23	0.544	0.488	0.531	0.529	0.490	0.521	0.694	0.511
alpha blockers	9	0.566	0.543	0.579	0.540	0.593	0.513	0.621	0.568
anti anxiety	287	0.643	0.532	0.627	0.540	0.572	0.518	0.689	0.564
anti psychotics	38	0.613	0.560	0.552	0.507	0.530	0.533	0.695	0.564
anticoagulants	35	0.687	0.565	0.678	0.576	0.736	0.589	0.717	0.612
antidepressants	306	0.672	0.558	0.675	0.566	0.681	0.566	0.767	0.621
antiplatelets	17	0.735	0.539	0.651	0.519	0.694	0.601	0.661	0.584
beta blockers	153	0.683	0.576	0.651	0.559	0.653	0.544	0.767	0.622
diuretics	120	0.649	0.549	0.703	0.589	0.728	0.585	0.754	0.594
minoxidil	75	0.602	0.498	0.590	0.507	0.606	0.529	0.635	0.544
none	617	0.634	0.522	0.622	0.519	0.646	0.532	0.666	0.528
opioid	27	0.662	0.545	0.567	0.568	0.642	0.528	0.784	0.642
sleeping aids	227	0.560	0.522	0.571	0.532	0.585	0.526	0.603	0.536
Mean (Treatment)	—	0.640	0.536	0.624	0.541	0.626	0.541	0.691	0.571
<i>Health Conditions</i>									
COPD	31	0.568	0.489	0.614	0.495	0.592	0.519	0.662	0.543
allergy	182	0.555	0.505	0.574	0.509	0.556	0.506	0.626	0.518
anxiety	420	0.675	0.558	0.671	0.540	0.620	0.531	0.741	0.586
arthritis	167	0.724	0.545	0.776	0.588	0.731	0.574	0.781	0.592
asthma	223	0.529	0.504	0.567	0.507	0.551	0.515	0.552	0.511
atrial fibrillation	42	0.755	0.647	0.757	0.629	0.763	0.622	0.757	0.622
back disorder	145	0.639	0.539	0.648	0.540	0.613	0.524	0.681	0.563
cancer	65	0.646	0.516	0.618	0.540	0.681	0.565	0.699	0.562
coronary artery disease	32	0.762	0.618	0.772	0.649	0.801	0.651	0.850	0.687
depression	422	0.669	0.556	0.657	0.553	0.648	0.534	0.724	0.590
diabetes	125	0.687	0.556	0.716	0.576	0.737	0.581	0.791	0.620
hearing loss	80	0.657	0.565	0.629	0.549	0.723	0.570	0.732	0.606
heart attack	24	0.800	0.682	0.756	0.612	0.798	0.617	0.854	0.677
heart failure	17	0.813	0.667	0.784	0.604	0.804	0.650	0.868	0.678
high cholesterol	593	0.559	0.511	0.562	0.516	0.594	0.511	0.601	0.513
high triglycerides	260	0.547	0.505	0.561	0.511	0.555	0.517	0.571	0.518
hypertension	743	0.665	0.544	0.676	0.562	0.690	0.552	0.719	0.578
joint replace.	32	0.766	0.614	0.727	0.600	0.790	0.636	0.847	0.636
kidney disease	60	0.556	0.565	0.570	0.544	0.615	0.542	0.673	0.544
neck disorder	65	0.616	0.528	0.513	0.519	0.558	0.518	0.664	0.574
neuropathy	52	0.688	0.563	0.669	0.573	0.665	0.545	0.741	0.597
none	348	0.605	0.533	0.639	0.535	0.660	0.540	0.678	0.547
osteoporosis	24	0.781	0.594	0.759	0.619	0.729	0.625	0.779	0.656
other rhythm	88	0.594	0.527	0.548	0.504	0.562	0.517	0.635	0.537
pacemaker	4	0.916	0.737	0.894	0.731	0.812	0.560	0.890	0.737
stroke	11	0.616	0.563	0.589	0.601	0.590	0.512	0.740	0.533
thyroid disease	96	0.632	0.527	0.673	0.528	0.658	0.538	0.686	0.548
urinary incontinence	20	0.700	0.517	0.769	0.614	0.743	0.596	0.809	0.648
valve disease	12	0.504	0.474	0.547	0.505	0.700	0.595	0.514	0.526
vision loss	40	0.538	0.512	0.508	0.507	0.463	0.498	0.649	0.540
Mean (Health Condition)	—	0.659	0.559	0.658	0.562	0.667	0.559	0.717	0.586
Overall Mean	—	0.667	0.565	0.658	0.567	0.661	0.561	0.719	0.595

Table 10 | Detailed performance comparison against PPG Foundation Models.

Task	# Pos	AnyPPG [13]		PulsePPG [12]		PaPaGei [11]		WavesFM	
		AUROC [†]	pAUC [†]	AUROC [†]	pAUC [†]	AUROC [†]	pAUC [†]	AUROC [†]	pAUC [†]
<i>Demographics</i>									
obesity (BMI \geq 30)	727	0.813	0.672	0.829	0.670	0.782	0.629	0.913	0.787
older age (age \geq 50)	447	0.902	0.743	0.901	0.730	0.854	0.720	0.951	0.829
sex male	1254	0.963	0.886	0.972	0.891	0.934	0.798	0.992	0.966
Mean (Demographics)	—	0.893	0.767	0.901	0.764	0.857	0.716	0.952	0.860
<i>Lifestyle</i>									
active smoker	107	0.622	0.559	0.622	0.542	0.576	0.528	0.765	0.599
always salt	94	0.596	0.503	0.584	0.509	0.578	0.505	0.593	0.520
freq alcohol	351	0.615	0.520	0.616	0.523	0.607	0.522	0.781	0.635
freq sugar	191	0.549	0.512	0.547	0.516	0.571	0.512	0.617	0.557
Mean (Lifestyle)	—	0.595	0.523	0.592	0.522	0.583	0.517	0.689	0.578
<i>Treatment</i>									
ACE inhib.	143	0.583	0.515	0.584	0.532	0.577	0.511	0.678	0.560
ARBs	198	0.592	0.525	0.599	0.529	0.582	0.527	0.715	0.561
CCBs	121	0.661	0.552	0.676	0.544	0.663	0.558	0.775	0.630
NSAIDs	393	0.557	0.505	0.564	0.504	0.539	0.508	0.561	0.513
PDE inhib.	91	0.468	0.503	0.572	0.516	0.455	0.502	0.655	0.516
aldosterone	23	0.663	0.531	0.616	0.544	0.635	0.501	0.694	0.511
alpha blockers	9	0.610	0.521	0.634	0.543	0.627	0.525	0.621	0.568
anti anxiety	287	0.641	0.543	0.640	0.533	0.591	0.517	0.689	0.564
anti psychotics	38	0.585	0.518	0.567	0.523	0.567	0.510	0.695	0.564
anticoagulants	35	0.612	0.547	0.579	0.551	0.621	0.602	0.717	0.612
antidepressants	306	0.649	0.541	0.695	0.562	0.653	0.538	0.767	0.621
antiplatelets	17	0.642	0.561	0.721	0.587	0.721	0.623	0.661	0.584
beta blockers	153	0.686	0.567	0.643	0.533	0.664	0.565	0.767	0.622
diuretics	120	0.658	0.542	0.646	0.532	0.589	0.542	0.754	0.594
minoxidil	75	0.579	0.520	0.591	0.531	0.574	0.510	0.635	0.544
none	617	0.627	0.525	0.627	0.524	0.599	0.520	0.666	0.528
opioid	27	0.655	0.549	0.699	0.562	0.658	0.561	0.784	0.642
sleeping aids	227	0.591	0.536	0.586	0.532	0.589	0.523	0.603	0.536
Mean (Treatment)	—	0.614	0.533	0.624	0.538	0.606	0.536	0.691	0.571
<i>Health Conditions</i>									
COPD	31	0.533	0.518	0.552	0.525	0.551	0.516	0.662	0.543
allergy	182	0.583	0.508	0.605	0.516	0.583	0.507	0.626	0.518
anxiety	420	0.639	0.537	0.671	0.527	0.653	0.532	0.741	0.586
arthritis	167	0.745	0.577	0.709	0.564	0.682	0.562	0.781	0.592
asthma	223	0.563	0.513	0.541	0.495	0.535	0.503	0.552	0.511
atrial fibrillation	42	0.738	0.637	0.627	0.555	0.620	0.549	0.757	0.622
back disorder	145	0.637	0.538	0.625	0.526	0.626	0.539	0.681	0.563
cancer	65	0.624	0.557	0.604	0.526	0.619	0.535	0.699	0.562
coronary artery disease	32	0.820	0.670	0.809	0.597	0.760	0.643	0.850	0.687
depression	422	0.637	0.536	0.649	0.540	0.659	0.535	0.724	0.590
diabetes	125	0.737	0.587	0.693	0.575	0.689	0.579	0.791	0.620
hearing loss	80	0.688	0.566	0.655	0.582	0.652	0.559	0.732	0.606
heart attack	24	0.764	0.614	0.723	0.548	0.722	0.567	0.854	0.677
heart failure	17	0.695	0.587	0.731	0.634	0.721	0.636	0.868	0.678
high cholesterol	593	0.563	0.513	0.541	0.510	0.552	0.511	0.601	0.513
high triglycerides	260	0.558	0.511	0.566	0.501	0.546	0.493	0.571	0.518
hypertension	743	0.650	0.554	0.672	0.573	0.661	0.556	0.719	0.578
joint replace.	32	0.836	0.606	0.724	0.591	0.770	0.590	0.847	0.636
kidney disease	60	0.619	0.542	0.628	0.569	0.595	0.559	0.673	0.544
neck disorder	65	0.481	0.495	0.579	0.531	0.563	0.516	0.664	0.574
neuropathy	52	0.650	0.534	0.701	0.543	0.641	0.537	0.741	0.597
none	348	0.642	0.536	0.628	0.533	0.607	0.529	0.678	0.547
osteoporosis	24	0.726	0.660	0.740	0.652	0.738	0.629	0.779	0.656
other rhythm	88	0.550	0.519	0.541	0.511	0.563	0.531	0.635	0.537
pacemaker	4	0.762	0.675	0.779	0.601	0.743	0.608	0.890	0.737
stroke	11	0.544	0.599	0.596	0.552	0.544	0.529	0.740	0.533
thyroid disease	96	0.678	0.561	0.642	0.568	0.658	0.567	0.686	0.548
urinary incontinence	20	0.622	0.562	0.713	0.553	0.606	0.534	0.809	0.648
valve disease	12	0.580	0.530	0.624	0.541	0.698	0.539	0.514	0.526
vision loss	40	0.507	0.520	0.565	0.527	0.562	0.515	0.649	0.540
Mean (Health Condition)	—	0.646	0.562	0.648	0.552	0.637	0.550	0.717	0.586
Overall Mean	—	0.645	0.561	0.650	0.557	0.635	0.552	0.719	0.595

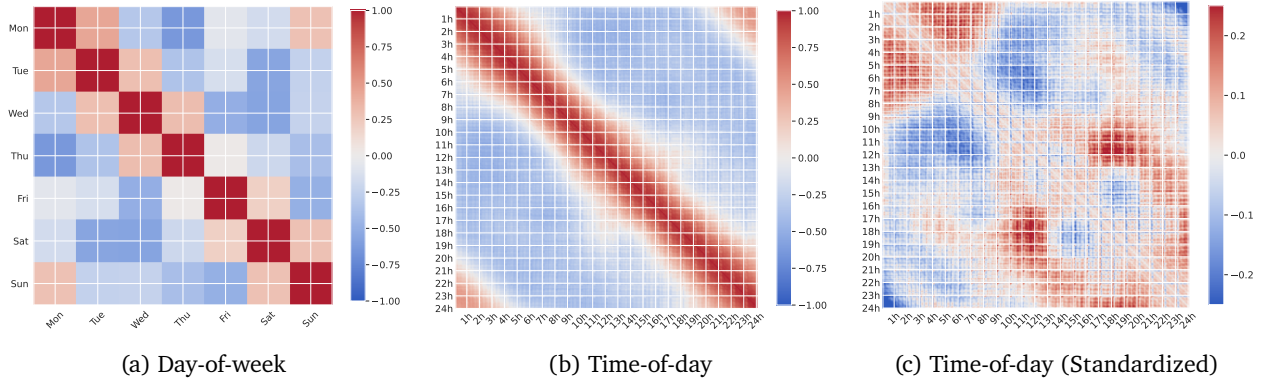
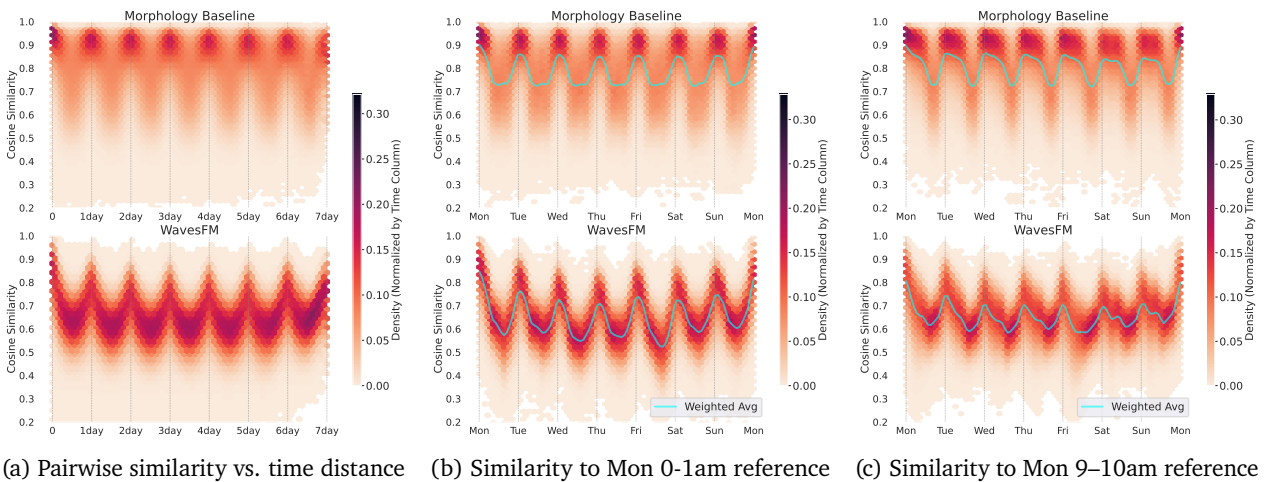


Figure 13 | Pairwise cosine similarity of factorized position embeddings.


 Figure 14 | **Supplementary analysis of circadian structure.** (a) Density of pairwise cosine similarities for all intra-subject segment pairs, plotted as a function of the time distance between the two segments. (b)(c) Density of pairwise cosine similarities across the week, calculated against each subject’s Monday 0–1am or 9-10am reference embeddings.

D.5. Latent Space Analyses

Factorized Positional Embedding Analyses We analyzed the factorized positional embeddings introduced in Section 3.2 by extracting the learned time-of-day (288 embeddings, 5-minute resolution) and day-of-week (7 embeddings, 1-day resolution) representations, computing their respective 288×288 and 7×7 pairwise cosine similarity matrices. The unnormalized time-of-day pairwise matrices (depicted in Figure 13) reveal strong temporal continuity, characterized by high similarity between adjacent temporal positions. However, the day-of-week embeddings exhibit a notable discontinuity between Thursday and Friday, potentially reflecting a shift in physiological rhythm at the end of the workweek.

To uncover latent variations obscured by the dominant diagonal continuity, we standardized the similarities by subtracting the mean similarity of pairs with identical time gaps. This normalized view reveals distinct physiological regimes: a low-similarity cluster (blue) separates the daytime window (9am–2pm) from the night (12am–9am), indicating highly divergent states. Conversely, high-similarity clusters (red) emerge between discrete time windows that align with specific physiological states, such as sleep cycles (12am–3am vs. 4am–7am) and synchronized metabolic or dietary routines (10am–1pm vs. 5pm–8pm).

Unpooled Segment Embedding Analyses Beyond positional embeddings, we directly analyze the similarities among unpooled segment embeddings to further evaluate the temporal encoder’s contribution. Plotting pairwise cosine similarities against temporal distance (Figure 14a) reveals a strong circadian rhythm in WavesFM that is notably less pronounced in the morphology-centric baseline. Additionally, when substituting the main text’s 9–10am reference with a 12–1am reference (Figure 14b), the baseline yields the same shallow, binary pattern, where a shorter plateau likely reflects a shorter nocturnal sleep duration relative to daytime activity. In contrast, WavesFM consistently captures a continuous, full-cycle circadian rhythm independent of the chosen reference time.

E. Ablation Experiments

Dual-Branch Ablation. To evaluate the Stage II dual branch’s contribution, we ablated the local and global branches independently, retraining each variant using identical hyperparameter sets to prevent checkpoint bias. By comparing the distribution of mean AUROCs across all hyperparameter configurations, we evaluated linear probing performance over five temporally restricted subsets (all, day, night, weekday, weekend) using 10% and 100% linear probing subsets. The dual-branch model consistently outperforms both single-branch baselines (Figure 15). This advantage widens significantly under data constraints, whether restricted at the subject level (e.g., using only 10% of subjects) or the segment level (e.g., night-only inputs), emphasizing that both branches are necessary for robust representations.

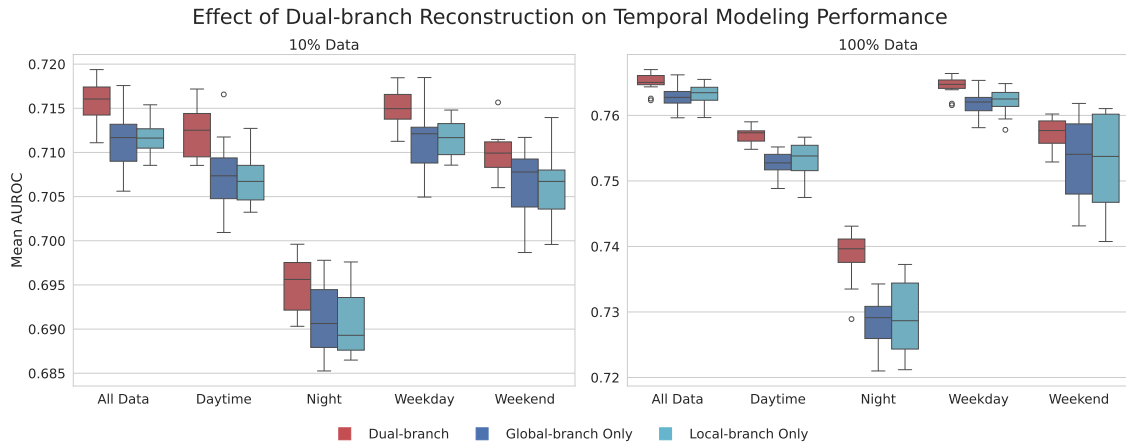


Figure 15 | Ablation of Dual-Branch Temporal Modeling

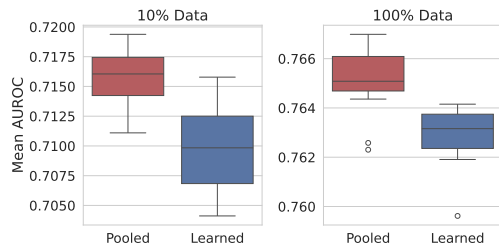


Figure 16 | Week-level Embedding Ablation

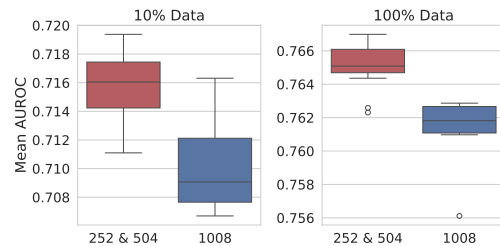


Figure 17 | Context Set Size Ablation

Week-level Embedding Ablation. We evaluated an average-pooled token against a dedicated learnable token to serve as the week-level representation in dual-branch training. The pooled embedding strategy demonstrates a consistent performance advantage over the learnable token across both the 10% and 100% linear probing subsets (Figure 16).

Context Set Size Ablation. We trained the temporal encoder using three different context set sizes ($N_{\text{ctx}} = 252, 504, \text{ and } 1008$), corresponding to 12.5%, 25%, and 50% of the total sequence length, respectively. We observe a significant performance advantage when using smaller context sizes (252 and 504) compared to the largest (1008) (Figure 17). This aligns with existing literature, which suggests that higher masking ratios yield more robust representations in masked reconstruction pretraining [45]. These performance gains saturate at a context size of 504 (25%) in our experiments, with no significant difference observed between the 252 and 504 configurations.